

# Absolute luminosity measurements with the LHCb detector at the LHC

---

## The LHCb Collaboration\*

**ABSTRACT:** Absolute luminosity measurements are of general interest for colliding-beam experiments at storage rings. These measurements are necessary to determine the absolute cross-sections of reaction processes and are valuable to quantify the performance of the accelerator. Using data taken in 2010, LHCb has applied two methods to determine the absolute scale of its luminosity measurements for proton-proton collisions at the LHC with a centre-of-mass energy of 7 TeV. In addition to the classic “van der Meer scan” method a novel technique has been developed which makes use of direct imaging of the individual beams using beam-gas and beam-beam interactions. This beam imaging method is made possible by the high resolution of the LHCb vertex detector and the close proximity of the detector to the beams, and allows beam parameters such as positions, angles and widths to be determined. The results of the two methods have comparable precision and are in good agreement. Combining the two methods, an overall precision of 3.5% in the absolute luminosity determination is reached. The techniques used to transport the absolute luminosity calibration to the full 2010 data-taking period are presented.

**KEYWORDS:** LHC; LHCb; luminosity; van der Meer; beam imaging.

---

\*Authors are listed on the following pages

---

## Contents

<b>1. Introduction</b>	<b>6</b>
<b>2. The LHCb detector</b>	<b>7</b>
<b>3. Relative normalization method</b>	<b>9</b>
<b>4. Bunch population measurements</b>	<b>11</b>
<b>5. The van der Meer scan (VDM) method</b>	<b>13</b>
5.1 Experimental conditions during the van der Meer scan	14
5.2 Cross-section determination	16
5.3 Systematic errors	20
5.3.1 Reproducibility of the luminosity at the nominal beam positions	20
5.3.2 Length scale calibration	21
5.3.3 Coupling between the $x$ and $y$ coordinates in the LHC beams	23
5.3.4 Cross check with the $z$ position of the luminous region	24
5.4 Results of the van der Meer scans	25
<b>6. The beam-gas imaging (BGI) method</b>	<b>25</b>
6.1 Data-taking conditions	27
6.2 Analysis and data selection procedure	28
6.3 Vertex resolution	29
6.4 Measurement of the beam profiles using the BGI method	31
6.5 Corrections and systematic errors	36
6.5.1 Vertex resolution	36
6.5.2 Time dependence and stability	36
6.5.3 Bias due to unequal beam sizes and beam offsets	37
6.5.4 Gas pressure gradient	37
6.5.5 Crossing angle effects	38
6.6 Results of the beam-gas imaging method	39
<b>7. Cross checks with the beam-beam imaging method</b>	<b>42</b>
<b>8. Results and conclusions</b>	<b>43</b>
<b>9. Acknowledgements</b>	<b>45</b>

---

## LHCb Collaboration

R. Aaij<sup>23</sup>, B. Adeva<sup>36</sup>, M. Adinolfi<sup>42</sup>, C. Adrover<sup>6</sup>, A. Affolder<sup>48</sup>, Z. Ajaltouni<sup>5</sup>, J. Albrecht<sup>37</sup>, F. Alessio<sup>37</sup>, M. Alexander<sup>47</sup>, G. Alkhazov<sup>29</sup>, P. Alvarez Cartelle<sup>36</sup>, A.A. Alves Jr<sup>22</sup>, S. Amato<sup>2</sup>, Y. Amhis<sup>38</sup>, J. Anderson<sup>39</sup>, R.B. Appleby<sup>50</sup>, O. Aquines Gutierrez<sup>10</sup>, F. Archilli<sup>18,37</sup>, L. Arrabito<sup>53</sup>, A. Artamonov<sup>34</sup>, M. Artuso<sup>52,37</sup>, E. Aslanides<sup>6</sup>, G. Auriemma<sup>22,m</sup>, S. Bachmann<sup>11</sup>, J.J. Back<sup>44</sup>, D.S. Bailey<sup>50</sup>, V. Balagura<sup>30,37</sup>, W. Baldini<sup>16</sup>, R.J. Barlow<sup>50</sup>, C. Barschel<sup>37</sup>, S. Barsuk<sup>7</sup>, W. Barter<sup>43</sup>, A. Bates<sup>47</sup>, C. Bauer<sup>10</sup>, Th. Bauer<sup>23</sup>, A. Bay<sup>38</sup>, I. Bediaga<sup>1</sup>, K. Belous<sup>34</sup>, I. Belyaev<sup>30,37</sup>, E. Ben-Haim<sup>8</sup>, M. Benayoun<sup>8</sup>, G. Bencivenni<sup>18</sup>, S. Benson<sup>46</sup>, J. Benton<sup>42</sup>, R. Bernet<sup>39</sup>, M.-O. Bettler<sup>17</sup>, M. van Beuzekom<sup>23</sup>, A. Bien<sup>11</sup>, S. Bifani<sup>12</sup>, A. Bizzeti<sup>17,h</sup>, P.M. Bjørnstad<sup>50</sup>, T. Blake<sup>49</sup>, F. Blanc<sup>38</sup>, C. Blanks<sup>49</sup>, J. Blouw<sup>11</sup>, S. Blusk<sup>52</sup>, A. Bobrov<sup>33</sup>, V. Bocci<sup>22</sup>, A. Bondar<sup>33</sup>, N. Bondar<sup>29</sup>, W. Bonivento<sup>15</sup>, S. Borghi<sup>47</sup>, A. Borgia<sup>52</sup>, T.J.V. Bowcock<sup>48</sup>, C. Bozzi<sup>16</sup>, T. Brambach<sup>9</sup>, J. van den Brand<sup>24</sup>, J. Bressieux<sup>38</sup>, D. Brett<sup>50</sup>, S. Brisbane<sup>51</sup>, M. Britsch<sup>10</sup>, T. Britton<sup>52</sup>, N.H. Brook<sup>42</sup>, H. Brown<sup>48</sup>, A. Büchler-Germann<sup>39</sup>, I. Burducea<sup>28</sup>, A. Bursche<sup>39</sup>, J. Buytaert<sup>37</sup>, S. Cadeddu<sup>15</sup>, J.M. Caicedo Carvajal<sup>37</sup>, O. Callot<sup>7</sup>, M. Calvi<sup>20,j</sup>, M. Calvo Gomez<sup>35,n</sup>, A. Camboni<sup>35</sup>, P. Campana<sup>18,37</sup>, A. Carbone<sup>14</sup>, G. Carboni<sup>21,k</sup>, R. Cardinale<sup>19,i,37</sup>, A. Cardini<sup>15</sup>, L. Carson<sup>36</sup>, K. Carvalho Akiba<sup>23</sup>, G. Casse<sup>48</sup>, M. Cattaneo<sup>37</sup>, M. Charles<sup>51</sup>, Ph. Charpentier<sup>37</sup>, N. Chiapolini<sup>39</sup>, K. Ciba<sup>37</sup>, X. Cid Vidal<sup>36</sup>, G. Ciezarek<sup>49</sup>, P.E.L. Clarke<sup>46,37</sup>, M. Clemencic<sup>37</sup>, H.V. Cliff<sup>43</sup>, J. Closier<sup>37</sup>, C. Coca<sup>28</sup>, V. Coco<sup>23</sup>, J. Cogan<sup>6</sup>, P. Collins<sup>37</sup>, F. Constantin<sup>28</sup>, G. Conti<sup>38</sup>, A. Contu<sup>51</sup>, A. Cook<sup>42</sup>, M. Coombes<sup>42</sup>, G. Corti<sup>37</sup>, G.A. Cowan<sup>38</sup>, R. Currie<sup>46</sup>, B. D'Almagne<sup>7</sup>, C. D'Ambrosio<sup>37</sup>, P. David<sup>8</sup>, I. De Bonis<sup>4</sup>, S. De Capua<sup>21,k</sup>, M. De Cian<sup>39</sup>, F. De Lorenzi<sup>12</sup>, J.M. De Miranda<sup>1</sup>, L. De Paula<sup>2</sup>, P. De Simone<sup>18</sup>, D. Decamp<sup>4</sup>, M. Deckenhoff<sup>9</sup>, H. Degaudenzi<sup>38,37</sup>, M. Deissenroth<sup>11</sup>, L. Del Buono<sup>8</sup>, C. Deplano<sup>15</sup>, O. Deschamps<sup>5</sup>, F. Dettori<sup>15,d</sup>, J. Dickens<sup>43</sup>, H. Dijkstra<sup>37</sup>, P. Diniz Batista<sup>1</sup>, S. Donleavy<sup>48</sup>, F. Dordei<sup>11</sup>, A. Dosil Suárez<sup>36</sup>, D. Dossett<sup>44</sup>, A. Dovbnya<sup>40</sup>, F. Dupertuis<sup>38</sup>, R. Dzhelyadin<sup>34</sup>, C. Eames<sup>49</sup>, S. Easo<sup>45</sup>, U. Egede<sup>49</sup>, V. Egorychev<sup>30</sup>, S. Eidelman<sup>33</sup>, D. van Eijk<sup>23</sup>, F. Eisele<sup>11</sup>, S. Eisenhardt<sup>46</sup>, R. Ekelhof<sup>9</sup>, L. Eklund<sup>47</sup>, Ch. Elsasser<sup>39</sup>, D.G. d'Enterria<sup>35,o</sup>, D. Esperante Pereira<sup>36</sup>, L. Estève<sup>43</sup>, A. Falabella<sup>16,e</sup>, E. Fanchini<sup>20,j</sup>, C. Färber<sup>11</sup>, G. Fardell<sup>46</sup>, C. Farinelli<sup>23</sup>, S. Farry<sup>12</sup>, V. Fave<sup>38</sup>, V. Fernandez Albor<sup>36</sup>, M. Ferro-Luzzi<sup>37</sup>, S. Filippov<sup>32</sup>, C. Fitzpatrick<sup>46</sup>, M. Fontana<sup>10</sup>, F. Fontanelli<sup>19,i</sup>, R. Forty<sup>37</sup>, M. Frank<sup>37</sup>, C. Frei<sup>37</sup>, M. Frosini<sup>17,f,37</sup>, S. Furcas<sup>20</sup>, A. Gallas Torreira<sup>36</sup>, D. Galli<sup>14,c</sup>, M. Gandelman<sup>2</sup>, P. Gandini<sup>51</sup>, Y. Gao<sup>3</sup>, J.-C. Garnier<sup>37</sup>, J. Garofoli<sup>52</sup>, J. Garra Tico<sup>43</sup>, L. Garrido<sup>35</sup>, C. Gaspar<sup>37</sup>, N. Gauvin<sup>38</sup>, M. Gersabeck<sup>37</sup>, T. Gershon<sup>44,37</sup>, Ph. Ghez<sup>4</sup>, V. Gibson<sup>43</sup>, V.V. Gligorov<sup>37</sup>, C. Göbel<sup>54</sup>, D. Golubkov<sup>30</sup>, A. Golutvin<sup>49,30,37</sup>, A. Gomes<sup>2</sup>, H. Gordon<sup>51</sup>, M. Grabalosa Gándara<sup>35</sup>, R. Graciani Diaz<sup>35</sup>, L.A. Granado Cardoso<sup>37</sup>, E. Graugés<sup>35</sup>, G. Graziani<sup>17</sup>, A. Greco<sup>28</sup>, S. Gregson<sup>43</sup>, B. Gui<sup>52</sup>, E. Gushchin<sup>32</sup>, Yu. Guz<sup>34</sup>, T. Gys<sup>37</sup>, G. Haefeli<sup>38</sup>, C. Haen<sup>37</sup>, S.C. Haines<sup>43</sup>, T. Hampson<sup>42</sup>, S. Hansmann-Menzemer<sup>11</sup>, R. Harji<sup>49</sup>, N. Harnew<sup>51</sup>, J. Harrison<sup>50</sup>, P.F. Harrison<sup>44</sup>, J. He<sup>7</sup>, V. Heijne<sup>23</sup>, K. Hennessy<sup>48</sup>, P. Henrard<sup>5</sup>, J.A. Hernando Morata<sup>36</sup>, E. van Herwijnen<sup>37</sup>, E. Hicks<sup>48</sup>, W. Hofmann<sup>10</sup>, K. Holubyev<sup>11</sup>, P. Hopchev<sup>4</sup>, W. Hulsbergen<sup>23</sup>, P. Hunt<sup>51</sup>, T. Huse<sup>48</sup>, R.S. Huston<sup>12</sup>, D. Hutchcroft<sup>48</sup>, D. Hynds<sup>47</sup>, V. Iakovenko<sup>41</sup>, P. Ilten<sup>12</sup>, J. Imong<sup>42</sup>, R. Jacobsson<sup>37</sup>, A. Jaeger<sup>11</sup>, M. Jahjah Hussein<sup>5</sup>, E. Jans<sup>23</sup>, F. Jansen<sup>23</sup>, P. Jaton<sup>38</sup>, B. Jean-Marie<sup>7</sup>, F. Jing<sup>3</sup>, M. John<sup>51</sup>, D. Johnson<sup>51</sup>, C.R. Jones<sup>43</sup>, B. Jost<sup>37</sup>, S. Kandybei<sup>40</sup>, M. Karacson<sup>37</sup>, T.M. Karbach<sup>9</sup>, J. Keaveney<sup>12</sup>, U. Kerzel<sup>37</sup>, T. Ketel<sup>24</sup>, A. Keune<sup>38</sup>, B. Khanji<sup>6</sup>, Y.M. Kim<sup>46</sup>, M. Knecht<sup>38</sup>,

S. Koblitz<sup>37</sup>, P. Koppenburg<sup>23</sup>, A. Kozlinskiy<sup>23</sup>, L. Kravchuk<sup>32</sup>, K. Kreplin<sup>11</sup>, M. Kreps<sup>44</sup>, G. Krockner<sup>11</sup>, P. Krovovny<sup>11</sup>, F. Kruse<sup>9</sup>, K. Kruzelecki<sup>37</sup>, M. Kucharczyk<sup>20,25,37</sup>, S. Kukulak<sup>25</sup>, R. Kumar<sup>14,37</sup>, T. Kvaratskheliya<sup>30,37</sup>, V.N. La Thi<sup>38</sup>, D. Lacarrere<sup>37</sup>, G. Lafferty<sup>50</sup>, A. Lai<sup>15</sup>, D. Lambert<sup>46</sup>, R.W. Lambert<sup>37</sup>, E. Lanciotti<sup>37</sup>, G. Lanfranchi<sup>18</sup>, C. Langenbruch<sup>11</sup>, T. Latham<sup>44</sup>, R. Le Gac<sup>6</sup>, J. van Leerdam<sup>23</sup>, J.-P. Lees<sup>4</sup>, R. Lefèvre<sup>5</sup>, A. Leflat<sup>31,37</sup>, J. Lefrançois<sup>7</sup>, O. Leroy<sup>6</sup>, T. Lesiak<sup>25</sup>, L. Li<sup>3</sup>, L. Li Gioi<sup>5</sup>, M. Lieng<sup>9</sup>, M. Liles<sup>48</sup>, R. Lindner<sup>37</sup>, C. Linn<sup>11</sup>, B. Liu<sup>3</sup>, G. Liu<sup>37</sup>, J.H. Lopes<sup>2</sup>, E. Lopez Asamar<sup>35</sup>, N. Lopez-March<sup>38</sup>, J. Luisier<sup>38</sup>, F. Machefert<sup>7</sup>, I.V. Machikhiliyan<sup>4,30</sup>, F. Maciuc<sup>10</sup>, O. Maev<sup>29,37</sup>, J. Magnin<sup>1</sup>, S. Malde<sup>51</sup>, R.M.D. Mamunur<sup>37</sup>, G. Manca<sup>15,d</sup>, G. Mancinelli<sup>6</sup>, N. Mangiafave<sup>43</sup>, U. Marconi<sup>14</sup>, R. Märki<sup>38</sup>, J. Marks<sup>11</sup>, G. Martellotti<sup>22</sup>, A. Martens<sup>7</sup>, L. Martin<sup>51</sup>, A. Martín Sánchez<sup>7</sup>, D. Martinez Santos<sup>37</sup>, A. Massafferri<sup>1</sup>, R. Matev<sup>37,p</sup>, Z. Mathe<sup>12</sup>, C. Matteuzzi<sup>20</sup>, M. Matveev<sup>29</sup>, E. Maurice<sup>6</sup>, B. Maynard<sup>52</sup>, A. Mazurov<sup>16,32,37</sup>, G. McGregor<sup>50</sup>, R. McNulty<sup>12</sup>, C. Mclean<sup>14</sup>, M. Meissner<sup>11</sup>, M. Merk<sup>23</sup>, J. Merkel<sup>9</sup>, R. Messi<sup>21,k</sup>, S. Miglioranza<sup>37</sup>, D.A. Milanese<sup>13,37</sup>, M.-N. Minard<sup>4</sup>, S. Monteil<sup>5</sup>, D. Moran<sup>12</sup>, P. Morawski<sup>25</sup>, R. Mountain<sup>52</sup>, I. Mous<sup>23</sup>, F. Muheim<sup>46</sup>, K. Müller<sup>39</sup>, R. Muresan<sup>28,38</sup>, B. Muryn<sup>26</sup>, M. Musy<sup>35</sup>, J. Mylroie-Smith<sup>48</sup>, P. Naik<sup>42</sup>, T. Nakada<sup>38</sup>, R. Nandakumar<sup>45</sup>, J. Nardulli<sup>45</sup>, I. Nasteva<sup>1</sup>, M. Nedos<sup>9</sup>, M. Needham<sup>46</sup>, N. Neufeld<sup>37</sup>, C. Nguyen-Mau<sup>38,q</sup>, M. Nicol<sup>7</sup>, S. Nies<sup>9</sup>, V. Niess<sup>5</sup>, N. Nikitin<sup>31</sup>, A. Oblakowska-Mucha<sup>26</sup>, V. Obraztsov<sup>34</sup>, S. Oggero<sup>23</sup>, S. Ogilvy<sup>47</sup>, O. Okhrimenko<sup>41</sup>, R. Oldeman<sup>15,d</sup>, M. Orlandea<sup>28</sup>, J.M. Otalora Goicochea<sup>2</sup>, P. Owen<sup>49</sup>, B. Pal<sup>52</sup>, J. Palacios<sup>39</sup>, M. Palutan<sup>18</sup>, J. Panman<sup>37</sup>, A. Papanestis<sup>45</sup>, M. Pappagallo<sup>13,b</sup>, C. Parkes<sup>47,37</sup>, C.J. Parkinson<sup>49</sup>, G. Passaleva<sup>17</sup>, G.D. Patel<sup>48</sup>, M. Patel<sup>49</sup>, S.K. Paterson<sup>49</sup>, G.N. Patrick<sup>45</sup>, C. Patrignani<sup>19,i</sup>, C. Pavel-Nicorescu<sup>28</sup>, A. Pazos Alvarez<sup>36</sup>, A. Pellegrino<sup>23</sup>, G. Penso<sup>22,l</sup>, M. Pepe Altarelli<sup>37</sup>, S. Perazzini<sup>14,c</sup>, D.L. Perego<sup>20,j</sup>, E. Perez Trigo<sup>36</sup>, A. Pérez-Calero Yzquierdo<sup>35</sup>, P. Perret<sup>5</sup>, M. Perrin-Terrin<sup>6</sup>, G. Pessina<sup>20</sup>, A. Petrella<sup>16,37</sup>, A. Petrolini<sup>19,i</sup>, B. Pie Valls<sup>35</sup>, B. Pietrzyk<sup>4</sup>, T. Pilar<sup>44</sup>, D. Pinci<sup>22</sup>, R. Plackett<sup>47</sup>, S. Playfer<sup>46</sup>, M. Plo Casasus<sup>36</sup>, G. Polok<sup>25</sup>, A. Poluektov<sup>44,33</sup>, E. Polcarpo<sup>2</sup>, D. Popov<sup>10</sup>, B. Popovici<sup>28</sup>, C. Potterat<sup>35</sup>, A. Powell<sup>51</sup>, T. du Pree<sup>23</sup>, J. Prisciandaro<sup>38</sup>, V. Pugatch<sup>41</sup>, A. Puig Navarro<sup>35</sup>, W. Qian<sup>52</sup>, J.H. Rademacker<sup>42</sup>, B. Rakotomiramanana<sup>38</sup>, M.S. Rangel<sup>2</sup>, I. Raniuk<sup>40</sup>, G. Raven<sup>24</sup>, S. Redford<sup>51</sup>, M.M. Reid<sup>44</sup>, A.C. dos Reis<sup>1</sup>, S. Ricciardi<sup>45</sup>, K. Rinnert<sup>48</sup>, D.A. Roa Romero<sup>5</sup>, P. Robbe<sup>7</sup>, E. Rodrigues<sup>47</sup>, F. Rodrigues<sup>2</sup>, P. Rodriguez Perez<sup>36</sup>, G.J. Rogers<sup>43</sup>, S. Roiser<sup>37</sup>, V. Romanovsky<sup>34</sup>, J. Rouvinet<sup>38</sup>, T. Ruf<sup>37</sup>, H. Ruiz<sup>35</sup>, G. Sabatino<sup>21,k</sup>, J.J. Saborido Silva<sup>36</sup>, N. Sagidova<sup>29</sup>, P. Sail<sup>47</sup>, B. Saitta<sup>15,d</sup>, C. Salzmann<sup>39</sup>, M. Sannino<sup>19,i</sup>, R. Santacesaria<sup>22</sup>, C. Santamarina Rios<sup>36</sup>, R. Santinelli<sup>37</sup>, E. Santovetti<sup>21,k</sup>, M. Sapunov<sup>6</sup>, A. Sarti<sup>18,l</sup>, C. Satriano<sup>22,m</sup>, A. Satta<sup>21</sup>, M. Savrie<sup>16,e</sup>, D. Savrina<sup>30</sup>, P. Schaack<sup>49</sup>, M. Schiller<sup>11</sup>, S. Schleich<sup>9</sup>, M. Schmelling<sup>10</sup>, B. Schmidt<sup>37</sup>, O. Schneider<sup>38</sup>, A. Schopper<sup>37</sup>, M.-H. Schune<sup>7</sup>, R. Schwemmer<sup>37</sup>, A. Sciubba<sup>18,l</sup>, M. Seco<sup>36</sup>, A. Semennikov<sup>30</sup>, K. Senderowska<sup>26</sup>, I. Sepp<sup>49</sup>, N. Serra<sup>39</sup>, J. Serrano<sup>6</sup>, P. Seyfert<sup>11</sup>, B. Shao<sup>3</sup>, M. Shapkin<sup>34</sup>, I. Shapoval<sup>40,37</sup>, P. Shatalov<sup>30</sup>, Y. Shcheglov<sup>29</sup>, T. Shears<sup>48</sup>, L. Shekhtman<sup>33</sup>, O. Shevchenko<sup>40</sup>, V. Shevchenko<sup>30</sup>, A. Shires<sup>49</sup>, R. Silva Coutinho<sup>54</sup>, H.P. Skottowe<sup>43</sup>, T. Skwarnicki<sup>52</sup>, A.C. Smith<sup>37</sup>, N.A. Smith<sup>48</sup>, K. Sobczak<sup>5</sup>, F.J.P. Soler<sup>47</sup>, A. Solomin<sup>42</sup>, F. Soomro<sup>49</sup>, B. Souza De Paula<sup>2</sup>, B. Spaan<sup>9</sup>, A. Sparkes<sup>46</sup>, P. Spradlin<sup>47</sup>, F. Stagni<sup>37</sup>, S. Stahl<sup>11</sup>, O. Steinkamp<sup>39</sup>, S. Stoica<sup>28</sup>, S. Stone<sup>52,37</sup>, B. Storaci<sup>23</sup>, M. Straticiu<sup>28</sup>, U. Straumann<sup>39</sup>, N. Styles<sup>46</sup>, V.K. Subbiah<sup>37</sup>, S. Swientek<sup>9</sup>, M. Szczekowski<sup>27</sup>, P. Szczypka<sup>38</sup>, T. Szumlak<sup>26</sup>, S. T'Jampens<sup>4</sup>, E. Teodorescu<sup>28</sup>, F. Teubert<sup>37</sup>, C. Thomas<sup>51,45</sup>, E. Thomas<sup>37</sup>, J. van Tilburg<sup>11</sup>, V. Tisserand<sup>4</sup>, M. Tobin<sup>39</sup>, S. Topp-Joergensen<sup>51</sup>, M.T. Tran<sup>38</sup>,

A. Tsaregorodtsev<sup>6</sup>, N. Tuning<sup>23</sup>, M. Ubeda Garcia<sup>37</sup>, A. Ukleja<sup>27</sup>, P. Urquijo<sup>52</sup>, U. Uwer<sup>11</sup>, V. Vagnoni<sup>14</sup>, G. Valenti<sup>14</sup>, R. Vazquez Gomez<sup>35</sup>, P. Vazquez Regueiro<sup>36</sup>, S. Vecchi<sup>16</sup>, J.J. Velthuis<sup>42</sup>, M. Veltri<sup>17,g</sup>, K. Vervink<sup>37</sup>, B. Viaud<sup>7</sup>, I. Videau<sup>7</sup>, X. Vilasis-Cardona<sup>35,n</sup>, J. Visniakov<sup>36</sup>, A. Vollhardt<sup>39</sup>, D. Voong<sup>42</sup>, A. Vorobyev<sup>29</sup>, H. Voss<sup>10</sup>, K. Wacker<sup>9</sup>, S. Wandernoth<sup>11</sup>, J. Wang<sup>52</sup>, D.R. Ward<sup>43</sup>, A.D. Webber<sup>50</sup>, D. Websdale<sup>49</sup>, M. Whitehead<sup>44</sup>, D. Wiedner<sup>11</sup>, L. Wiggers<sup>23</sup>, G. Wilkinson<sup>51</sup>, M.P. Williams<sup>44,45</sup>, M. Williams<sup>49</sup>, F.F. Wilson<sup>45</sup>, J. Wishahi<sup>9</sup>, M. Witek<sup>25,37</sup>, W. Witzeling<sup>37</sup>, S.A. Wotton<sup>43</sup>, K. Wyllie<sup>37</sup>, Y. Xie<sup>46</sup>, F. Xing<sup>51</sup>, Z. Yang<sup>3</sup>, R. Young<sup>46</sup>, O. Yushchenko<sup>34</sup>, M. Zavertyaev<sup>10,a</sup>, F. Zhang<sup>3</sup>, L. Zhang<sup>52</sup>, W.C. Zhang<sup>12</sup>, Y. Zhang<sup>3</sup>, A. Zhelezov<sup>11</sup>, L. Zhong<sup>3</sup>, E. Zverev<sup>31</sup>, A. Zvyagin<sup>37</sup>.

<sup>1</sup>*Centro Brasileiro de Pesquisas Físicas (CBPF), Rio de Janeiro, Brazil*

<sup>2</sup>*Universidade Federal do Rio de Janeiro (UFRJ), Rio de Janeiro, Brazil*

<sup>3</sup>*Center for High Energy Physics, Tsinghua University, Beijing, China*

<sup>4</sup>*LAPP, Université de Savoie, CNRS/IN2P3, Annecy-Le-Vieux, France*

<sup>5</sup>*Clermont Université, Université Blaise Pascal, CNRS/IN2P3, LPC, Clermont-Ferrand, France*

<sup>6</sup>*CPPM, Aix-Marseille Université, CNRS/IN2P3, Marseille, France*

<sup>7</sup>*LAL, Université Paris-Sud, CNRS/IN2P3, Orsay, France*

<sup>8</sup>*LPNHE, Université Pierre et Marie Curie, Université Paris Diderot, CNRS/IN2P3, Paris, France*

<sup>9</sup>*Fakultät Physik, Technische Universität Dortmund, Dortmund, Germany*

<sup>10</sup>*Max-Planck-Institut für Kernphysik (MPIK), Heidelberg, Germany*

<sup>11</sup>*Physikalisches Institut, Ruprecht-Karls-Universität Heidelberg, Heidelberg, Germany*

<sup>12</sup>*School of Physics, University College Dublin, Dublin, Ireland*

<sup>13</sup>*Sezione INFN di Bari, Bari, Italy*

<sup>14</sup>*Sezione INFN di Bologna, Bologna, Italy*

<sup>15</sup>*Sezione INFN di Cagliari, Cagliari, Italy*

<sup>16</sup>*Sezione INFN di Ferrara, Ferrara, Italy*

<sup>17</sup>*Sezione INFN di Firenze, Firenze, Italy*

<sup>18</sup>*Laboratori Nazionali dell'INFN di Frascati, Frascati, Italy*

<sup>19</sup>*Sezione INFN di Genova, Genova, Italy*

<sup>20</sup>*Sezione INFN di Milano Bicocca, Milano, Italy*

<sup>21</sup>*Sezione INFN di Roma Tor Vergata, Roma, Italy*

<sup>22</sup>*Sezione INFN di Roma La Sapienza, Roma, Italy*

<sup>23</sup>*Nikhef National Institute for Subatomic Physics, Amsterdam, Netherlands*

<sup>24</sup>*Nikhef National Institute for Subatomic Physics and Vrije Universiteit, Amsterdam, Netherlands*

<sup>25</sup>*Henryk Niewodniczanski Institute of Nuclear Physics Polish Academy of Sciences, Cracow, Poland*

<sup>26</sup>*Faculty of Physics & Applied Computer Science, Cracow, Poland*

<sup>27</sup>*Soltan Institute for Nuclear Studies, Warsaw, Poland*

<sup>28</sup>*Horia Hulubei National Institute of Physics and Nuclear Engineering, Bucharest-Magurele, Romania*

<sup>29</sup>*Petersburg Nuclear Physics Institute (PNPI), Gatchina, Russia*

<sup>30</sup>*Institute of Theoretical and Experimental Physics (ITEP), Moscow, Russia*

<sup>31</sup>*Institute of Nuclear Physics, Moscow State University (SINP MSU), Moscow, Russia*

<sup>32</sup>*Institute for Nuclear Research of the Russian Academy of Sciences (INR RAN), Moscow, Russia*

<sup>33</sup>*Budker Institute of Nuclear Physics (SB RAS) and Novosibirsk State University, Novosibirsk, Russia*

<sup>34</sup>*Institute for High Energy Physics (IHEP), Protvino, Russia*

<sup>35</sup>*Universitat de Barcelona, Barcelona, Spain*

<sup>36</sup>*Universidad de Santiago de Compostela, Santiago de Compostela, Spain*

<sup>37</sup>*European Organization for Nuclear Research (CERN), Geneva, Switzerland*

<sup>38</sup>*Ecole Polytechnique Fédérale de Lausanne (EPFL), Lausanne, Switzerland*

<sup>39</sup>*Physik-Institut, Universität Zürich, Zürich, Switzerland*

<sup>40</sup>*NSC Kharkiv Institute of Physics and Technology (NSC KIPT), Kharkiv, Ukraine*

- <sup>41</sup>*Institute for Nuclear Research of the National Academy of Sciences (KINR), Kyiv, Ukraine*  
<sup>42</sup>*H.H. Wills Physics Laboratory, University of Bristol, Bristol, United Kingdom*  
<sup>43</sup>*Cavendish Laboratory, University of Cambridge, Cambridge, United Kingdom*  
<sup>44</sup>*Department of Physics, University of Warwick, Coventry, United Kingdom*  
<sup>45</sup>*STFC Rutherford Appleton Laboratory, Didcot, United Kingdom*  
<sup>46</sup>*School of Physics and Astronomy, University of Edinburgh, Edinburgh, United Kingdom*  
<sup>47</sup>*School of Physics and Astronomy, University of Glasgow, Glasgow, United Kingdom*  
<sup>48</sup>*Oliver Lodge Laboratory, University of Liverpool, Liverpool, United Kingdom*  
<sup>49</sup>*Imperial College London, London, United Kingdom*  
<sup>50</sup>*School of Physics and Astronomy, University of Manchester, Manchester, United Kingdom*  
<sup>51</sup>*Department of Physics, University of Oxford, Oxford, United Kingdom*  
<sup>52</sup>*Syracuse University, Syracuse, NY, United States*  
<sup>53</sup>*CC-IN2P3, CNRS/IN2P3, Lyon-Villeurbanne, France, associated member*  
<sup>54</sup>*Pontifícia Universidade Católica do Rio de Janeiro (PUC-Rio), Rio de Janeiro, Brazil, associated to <sup>2</sup>*

<sup>a</sup>*P.N. Lebedev Physical Institute, Russian Academy of Science (LPI RAS), Moscow, Russia*

<sup>b</sup>*Università di Bari, Bari, Italy*

<sup>c</sup>*Università di Bologna, Bologna, Italy*

<sup>d</sup>*Università di Cagliari, Cagliari, Italy*

<sup>e</sup>*Università di Ferrara, Ferrara, Italy*

<sup>f</sup>*Università di Firenze, Firenze, Italy*

<sup>g</sup>*Università di Urbino, Urbino, Italy*

<sup>h</sup>*Università di Modena e Reggio Emilia, Modena, Italy*

<sup>i</sup>*Università di Genova, Genova, Italy*

<sup>j</sup>*Università di Milano Bicocca, Milano, Italy*

<sup>k</sup>*Università di Roma Tor Vergata, Roma, Italy*

<sup>l</sup>*Università di Roma La Sapienza, Roma, Italy*

<sup>m</sup>*Università della Basilicata, Potenza, Italy*

<sup>n</sup>*LIFAELS, La Salle, Universitat Ramon Llull, Barcelona, Spain*

<sup>o</sup>*Institució Catalana de Recerca i Estudis Avançats (ICREA), Barcelona, Spain*

<sup>p</sup>*University of Sofia, Sofia, Bulgaria*

<sup>q</sup>*Hanoi University of Science, Hanoi, Viet Nam*

## 1. Introduction

Absolute luminosity measurements are of general interest to colliding-beam experiments at storage rings. Such measurements are necessary to determine the absolute cross-sections of reaction processes and to quantify the performance of the accelerator. The required accuracy on the value of the cross-section depends on both the process of interest and the precision of the theoretical predictions. At the LHC, the required precision on the cross-section is expected to be of order 1–2%. This estimate is motivated by the accuracy of theoretical predictions for the production of vector bosons and for the two-photon production of muon pairs [1–4].

In a cyclical collider, such as the LHC, the average instantaneous luminosity of one pair of colliding bunches can be expressed as [5]

$$L = N_1 N_2 f \sqrt{(\vec{v}_1 - \vec{v}_2)^2 - \frac{(\vec{v}_1 \times \vec{v}_2)^2}{c^2}} \int \rho_1(x, y, z, t) \rho_2(x, y, z, t) dx dy dz dt, \quad (1.1)$$

where we have introduced the revolution frequency  $f$  (11245 Hz at the LHC), the numbers of protons  $N_1$  and  $N_2$  in the two bunches, the corresponding velocities  $\vec{v}_1$  and  $\vec{v}_2$  of the particles,<sup>1</sup> and the particle densities for beam 1 and beam 2,  $\rho_{1,2}(x, y, z, t)$ . The particle densities are normalized such that their individual integrals over all space are unity. For highly relativistic beams colliding with a very small half crossing-angle  $\alpha$ , the Møller factor  $\sqrt{(\vec{v}_1 - \vec{v}_2)^2 - (\vec{v}_1 \times \vec{v}_2)^2/c^2}$  reduces to  $2c \cos^2 \alpha \simeq 2c$ . The integral in Eq. 1.1 is known as the beam overlap integral.

Methods for absolute luminosity determination are generally classified as either direct or indirect. Indirect methods are *e.g.* the use of the optical theorem to make a simultaneous measurement of the elastic and total cross-sections [6, 7], or the comparison to a process of which the absolute cross-section is known, either from theory or by a previous direct measurement. Direct measurements make use of Eq. 1.1 and employ several strategies to measure the various parameters in the equation.

The analysis described in this paper relies on two direct methods to determine the absolute luminosity calibration: the “van der Meer scan” method (VDM) [8, 9] and the “beam-gas imaging” method (BGI) [10]. The BGI method is based on reconstructing beam-gas interaction vertices to measure the beam angles, positions and shapes. It was applied for the first time in LHCb (see Refs. [11–13]) using the first LHC data collected at the end of 2009 at  $\sqrt{s} = 900$  GeV. The BGI method relies on the high precision of the measurement of interaction vertices obtained with the LHCb vertex detector. The VDM method exploits the ability to move the beams in both transverse coordinates with high precision and to thus scan the colliding beams with respect to each other. This method is also being used by other LHC experiments [14]. The method was first applied at the CERN ISR [8]. Recently it was demonstrated that additional information can be extracted when the two beams probe each other such as during a VDM scan, allowing the individual beam profiles to be determined by using vertex measurements of  $pp$  interactions in beam-beam collisions (beam-beam imaging) [15].

In principle, beam profiles can also be obtained by scanning wires across the beams [16] or by inferring the beam properties by theoretical calculation from the beam optics. Both methods lack precision, however, as they both rely on detailed knowledge of the beam optics. The wire-scan

---

<sup>1</sup>In the approximation of zero emittance the velocities are the same within one bunch.

method is limited by the achievable proximity of the wire to the interaction region which introduces the dependence on the beam optics model.

The LHC operated with a  $pp$  centre-of-mass energy of 7 TeV (3.5 TeV per beam). Typical values observed for the transverse beam sizes are close to 50  $\mu\text{m}$  and 55 mm for the bunch length. The half-crossing angle was typically 0.2 mrad.

Data taken with the LHCb detector, located at interaction point (IP) 8, are used in conjunction with data from the LHC beam instrumentation. The measurements obtained with the VDM and BGI methods are found to be consistent, and an average is made for the final result. The limiting systematics in both measurements come from the knowledge of the bunch populations  $N_1$  and  $N_2$ . All other sources of systematics are specific to the analysis method. Therefore, the comparison of both methods provides an important cross check of the results. The beam-beam imaging method is applied to the data taken during the VDM scan as an overall cross check of the absolute luminosity measurement.

Since the absolute calibration can only be performed during specific running periods, a relative normalization method is needed to transport the results of the absolute calibration of the luminosity to the complete data-taking period. To this end we defined a class of visible interactions. The cross-section for these interactions is determined using the measurements of the absolute luminosity during specific data-taking periods. Once this visible cross-section is determined, the integrated luminosity for a period of data-taking is obtained by accumulating the count rate of the corresponding visible interactions over this period. Thus, the calibration of the absolute luminosity is translated into a determination of a well defined visible cross-section.

In the present paper we first describe briefly the LHCb detector in Sect. 2, and in particular those aspects relevant to the analysis presented here. In Sect. 3 the methods used for the relative normalization technique are given. The determination of the number of protons in the LHC bunches is detailed in Sect. 4. The two methods which are used to determine the absolute scale are described in Sect. 5 and 6, respectively. The cross checks made with the beam-beam imaging method are shown in Sect. 7. Finally, the results are combined in Sect. 8.

## 2. The LHCb detector

The LHCb detector is a magnetic dipole spectrometer with a polar angular coverage of approximately 10 to 300 mrad in the horizontal (bending) plane, and 10 to 250 mrad in the vertical plane. It is described in detail elsewhere [17]. A right-handed coordinate system is defined with its origin at the nominal  $pp$  interaction point, the  $z$  axis along the average nominal beam line and pointing towards the magnet, and the  $y$  axis pointing upwards. Beam 1 (beam 2) travels in the direction of positive (negative)  $z$ .

The apparatus contains tracking detectors, ring-imaging Cherenkov detectors, calorimeters, and a muon system. The tracking system comprises the vertex locator (VELO) surrounding the  $pp$  interaction region, a tracking station upstream of the dipole magnet and three tracking stations located downstream of the magnet. Particles traversing the spectrometer experience a bending-field integral of around 4 Tm.

The VELO plays an essential role in the application of the beam-gas imaging method at LHCb. It consists of two retractable halves, each having 21 modules of radial and azimuthal silicon-strip



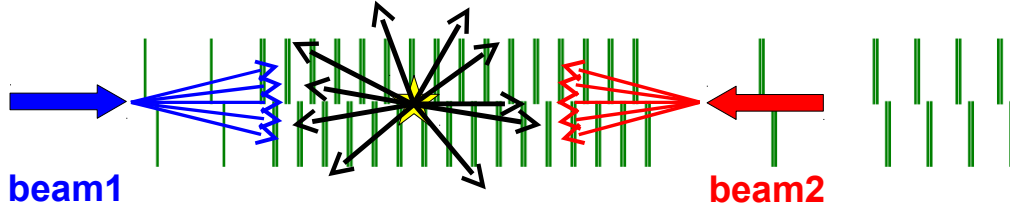


**Figure 1.** A sketch of the VELO, including the two Pile-Up stations on the left. The VELO sensors are drawn as double lines while the PU sensors are indicated with single lines. The thick arrows indicate the direction of the LHC beams (beam 1 going from left to right), while the thin ones show example directions of flight of the products of the beam-gas and beam-beam interactions.

sensors in a half-circle shape, see Fig. 1. Two additional stations (*Pile-Up System*, PU) upstream of the VELO tracking stations are mainly used in the hardware trigger. The VELO has a large acceptance for beam-beam interactions owing to its many layers of silicon sensors and their close proximity to the beam line. During nominal operation, the distance between sensor and beam is only 8 mm. During injection and beam adjustments, the two VELO halves are moved apart in a retracted position away from the beams. They are brought to their nominal position close to the beams during stable beam periods only.

The LHCb trigger system consists of two separate levels: a hardware trigger (L0), which is implemented in custom electronics, and a software High Level Trigger (HLT), which is executed on a farm of commercial processors. The L0 trigger system is designed to run at 1 MHz and uses information from the Pile-Up sensors of the VELO, the calorimeters and the muon system. They send information to the L0 decision unit (L0DU) where selection algorithms are run synchronously with the 40 MHz LHC bunch-crossing signal. For every nominal bunch-crossing slot (*i.e.* each 25 ns) the L0DU sends decisions to the LHCb readout supervisor. The full event information of all sub-detectors is available to the HLT algorithms.

A trigger strategy is adopted to select  $pp$  inelastic interactions and collisions of the beam with the residual gas in the vacuum chamber. Events are collected for the four bunch-crossing types: two colliding bunches (bb), one beam 1 bunch with no beam 2 bunch (be), one beam 2 bunch with no beam 1 bunch (eb) and nominally empty bunch slots (ee). Here “b” stands for “beam” and “e” stands for “empty”. The first two categories of crossings, which produce particles in the forward direction, are triggered using calorimeter information. An additional PU veto is applied for be crossings. Crossings of the type eb, which produce particles in the backward direction, are triggered by demanding a minimal hit multiplicity in the PU, and vetoed by calorimeter activity. The trigger for ee crossings is defined as the logical OR of the conditions used for the be and eb crossings in order to be sensitive to background from both beams. During VDM scans specialized trigger conditions are defined which optimize the data taking for these measurements (see Sect. 5.1).

The precise reconstruction of interaction vertices (“primary vertices”, PV) is an essential ingredient in the analysis described in this paper. The initial estimate of the PV position is based on an iterative clustering of tracks (“seeding”). Only tracks with hits in the VELO are considered. For each track the distance of closest approach (DOCA) with all other tracks is calculated and tracks are clustered into a seed if their DOCA is less than 1 mm. The position of the seed is then obtained using an iterative procedure. The point of closest approach between all track pairs is calculated and

its coordinates are used to discard outliers and to determine the weighted average position. The final PV coordinates are determined by iteratively improving the seed position with an adaptive, weighted, least-squares fit. In each iteration a new PV position is evaluated. Participating tracks are extrapolated to the  $z$  coordinate of the PV and assigned weights depending on their impact parameter with respect to the PV. The procedure is repeated for all seeds, excluding tracks from previously reconstructed primary vertices, retaining only PVs with at least five tracks. For this analysis only PVs with a larger number of tracks are used since they have better resolution. For the study of beam-gas interactions only PVs with at least ten tracks are used and at least 25 tracks are required for the study of  $pp$  interactions.

### 3. Relative normalization method

The absolute luminosity is obtained only for short periods of data-taking. To be able to perform cross-section measurements on any selected data sample, the relative luminosity must be measured consistently during the full period of data taking. The systematic relative normalization of all data-taking periods requires specific procedures to be applied in the trigger, data-acquisition, processing and final analysis. The basic principle is to acquire luminosity data together with the physics data and to store it in the same files as the physics event data. During further processing of the physics data the relevant luminosity data is kept together in the same storage entity. In this way, it remains possible to select only part of the full data-set for analysis and still keep the capability to determine the corresponding integrated luminosity.

The luminosity is proportional to the average number of visible proton-proton interactions in a beam-beam crossing,  $\mu_{\text{vis}}$ . The subscript “vis” is used to indicate that this holds for an arbitrary definition of the visible cross-section. Any stable interaction rate can be used as relative luminosity monitor. For a given period of data-taking, the integrated interaction rate can be used to determine the integrated luminosity if the cross-section for these visible interactions is known. The determination of the cross-section corresponding to these visible interactions is achieved by calibrating the absolute luminosity during specific periods and simultaneously counting the visible interactions.

Triggers which initiate the full readout of the LHCb detector are created for random beam crossings. These are called “luminosity triggers”. During normal physics data-taking, the overall rate is chosen to be 997 Hz, with 70% assigned to bb, 15% to be, 10% to eb and the remaining 5% to ee crossings. The events taken for crossing types other than bb are used for background subtraction and beam monitoring. After a processing step in the HLT a small number of “luminosity counters” are stored for each of these random luminosity triggers. The set of luminosity counters comprise the number of vertices and tracks in the VELO, the number of hits in the PU and in the scintillator pad detector (SPD) in front of calorimeters, and the transverse energy deposition in the calorimeters. Some of these counters are directly obtained from the L0, others are the result of partial event-reconstruction in the HLT.

During the final analysis stage the event data and luminosity data are available on the same files. The luminosity counters are summed (when necessary after time-dependent calibration) and an absolute calibration factor is applied to obtain the absolute integrated luminosity. The absolute calibration factor is universal and is the result of the luminosity calibration procedure described in this paper.

The relative luminosity can be determined by summing the values of any counter which is linear with the instantaneous luminosity. Alternatively, one may determine the relative luminosity from the fraction of “empty” or invisible events in bb crossings which we denote by  $P_0$ . An invisible event is defined by applying a counter-specific threshold below which it is considered that no  $pp$  interaction was seen in the corresponding bunch crossing. Since the number of events per bunch crossing follows a Poisson distribution with mean value proportional to the luminosity, the luminosity is proportional to  $-\ln P_0$ . This “zero count” method is both robust and easy to implement [18]. In the absence of backgrounds, the average number of visible  $pp$  interactions per crossing can be obtained from the fraction of empty bb crossings by  $\mu_{\text{vis}} = -\ln P_0^{\text{bb}}$ . Backgrounds are subtracted using

$$\mu_{\text{vis}} = - \left( \ln P_0^{\text{bb}} - \ln P_0^{\text{be}} - \ln P_0^{\text{eb}} + \ln P_0^{\text{ee}} \right), \quad (3.1)$$

where  $P_0^i$  ( $i = \text{bb}, \text{ee}, \text{be}, \text{eb}$ ) are the probabilities to find an empty event in a bunch-crossing slot for the four different bunch-crossing types. The  $P_0^{\text{ee}}$  contribution is added because it is also contained in the  $P_0^{\text{be}}$  and  $P_0^{\text{eb}}$  terms. The purpose of the background subtraction, Eq. 3.1, is to correct the count-rate in the bb crossings for the detector response which is due to beam-gas interactions and detector noise. In principle, the noise background is measured during ee crossings. In the presence of parasitic beam protons in ee bunch positions, as will be discussed below, it is not correct to evaluate the noise from  $P_0^{\text{ee}}$ . In addition, the detector signals are not fully confined within one 25 ns bunch-crossing slot. The empty (ee) bunch-crossing slots immediately following a bb, be or eb crossing slot contain detector signals from interactions occurring in the preceding slot (“spill-over”). The spill-over background is not present in the bb, be and eb crossings. Therefore, since the detector noise for the selected counters is small ( $< 10^{-5}$  relative to the typical values measured during bb crossings) the term  $\ln P_0^{\text{ee}}$  in Eq. 3.1 is neglected. Equation 3.1 assumes that the proton populations in the be and eb crossings are the same as in the bb crossings. With a population spread of typically 10% and a beam-gas background fraction  $< 10^{-4}$  compared to the  $pp$  interactions the effect of the spread is negligible, and is not taken into account.

The results of the zero-count method based on the number of hits in the PU and on the number of tracks in the VELO are found to be the most stable ones. An empty event is defined to have  $< 2$  hits when the PU is considered or  $< 2$  tracks when the VELO is considered. A VELO track is defined by at least three hits on a straight line in the radial strips of the silicon detectors of the VELO. The number of tracks reconstructed in the VELO is chosen as the most stable counter. In the following we will use the notation  $\sigma_{\text{vis}}$  ( $= \sigma_{\text{VELO}}$ ) for the visible cross-section measured using this method, except when explicitly stated otherwise. Modifications and alignment variations of the VELO also have negligible impact on the method, since the efficiency for reconstructing at least two tracks in an inelastic event is very stable against detector effects. Therefore, the systematics associated with this choice of threshold is negligible. The stability of the counter is demonstrated in Fig. 2 which shows the ratio of the relative luminosities determined with the zero-count method from the multiplicity of hits in the PU and from the number of VELO tracks. Apart from a few threshold updates in the PU configuration, the PU was also stable throughout LHCb 2010 running, and it was used as a cross check. Figure 3 covers the whole period of LHCb operation in 2010, with both low and high number of interactions per crossing. Similar cross checks have been made with the counter based on the number of reconstructed vertices. These three counters have different

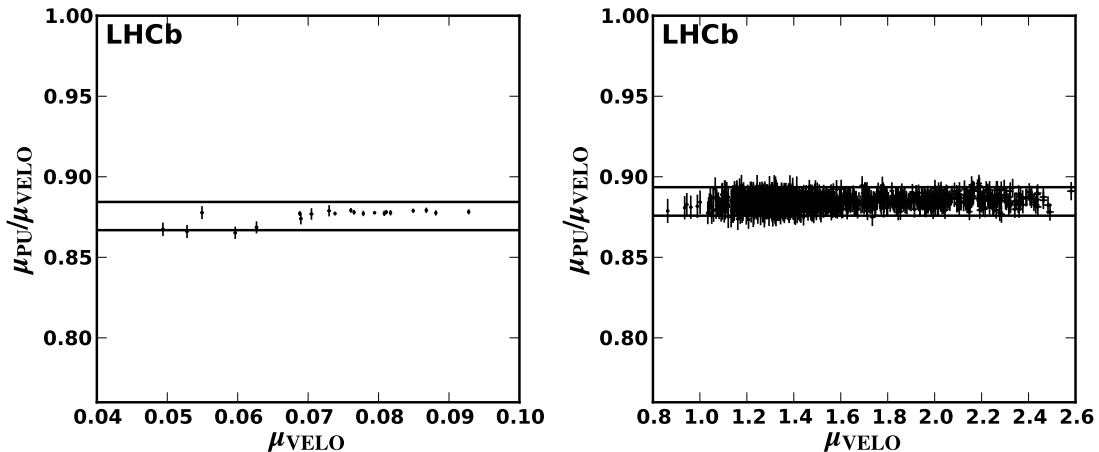


**Figure 2.** Ratio between  $\mu_{\text{vis}}$  values obtained with the zero-count method using the number of hits in the PU and the track count in the VELO versus  $\mu_{\text{VELO}}$ . The deviation from unity is due to the difference in acceptance. The left (right) panel uses runs from the beginning (end) of the 2010 running period with lower (higher) values of  $\mu_{\text{VELO}}$ . The horizontal lines indicate a  $\pm 1\%$  variation.

systematics, and by comparing their ratio as a function of time and instantaneous luminosity we conclude that the relative luminosity measurement has a systematic error of 0.5%.

The number of protons, beam sizes and transverse offsets at the interaction point vary across bunches. Thus, the  $\mu_{\text{vis}}$  value varies across bb bunch crossings. The spread in  $\mu_{\text{vis}}$  is about 10% of the mean value for typical runs. Due to the non-linearity of the logarithm function one first needs to compute  $\mu_{\text{vis}}$  values for different bunch crossings and then to take the average. However, for short time intervals the statistics are insufficient to distinguish between bunch-crossing IDs, while one cannot assume  $\mu_{\text{vis}}$  to be constant when the intervals are too long due to *e.g.* loss of bunch population and emittance growth. If the spread in instantaneous  $\mu_{\text{vis}}$  is known, the effect of neglecting it in calculating an average value of  $\mu_{\text{vis}}$  can be estimated. The difference between the naively computed  $\mu_{\text{vis}}$  value and the true one is then

$$\mu_{\text{vis}}^{\text{biased}} - \mu_{\text{vis}}^{\text{true}} = -\ln\langle P_0^i \rangle - (-\langle \ln P_0^i \rangle) = \langle \ln\left(\frac{P_0^i}{\langle P_0^i \rangle}\right) \rangle, \quad (3.2)$$

where the average is taken over all beam-beam crossing slots  $i$ . Therefore, the biased  $\mu_{\text{vis}}$  value can be calculated over short time intervals and a correction for the spread of  $\mu_{\text{vis}}$  can in principle be applied by computing  $P_0^i/\langle P_0^i \rangle$  over long time intervals. At the present level of accuracy, this correction is not required.<sup>2</sup> The effect is only weakly dependent on the luminosity counter used.

#### 4. Bunch population measurements

To measure the number of particles in the LHC beams two types of beam current transformers are installed in each ring [19]. One type, the DCCT (DC Current Transformer), measures the total current of the beams. The other type, the FBCT (Fast Beam Current Transformer), is gated with

<sup>2</sup>The relative luminosity increases by 0.5% when the correction is applied.

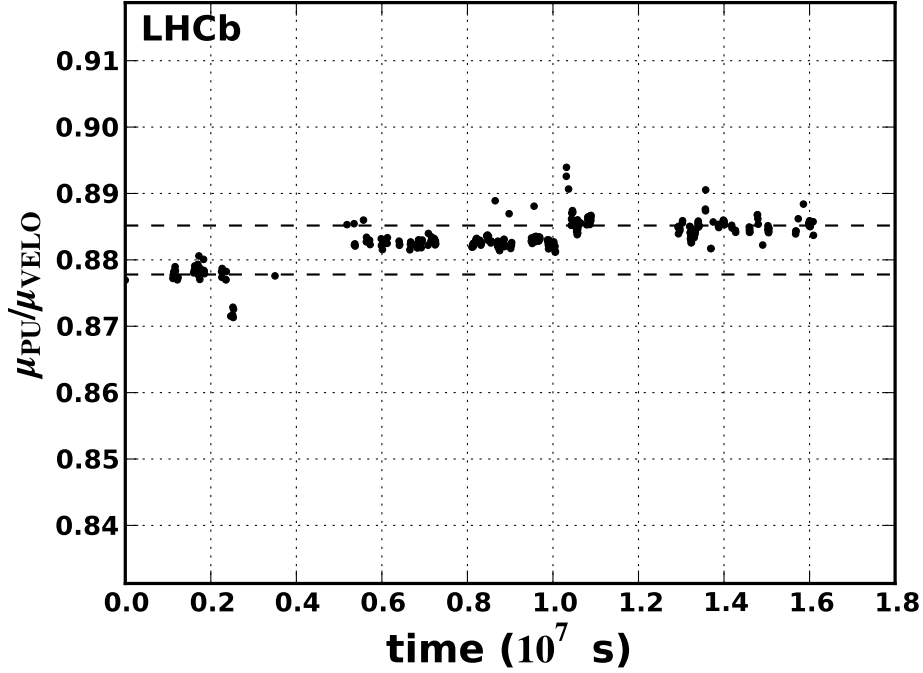


**Figure 3.** Ratio between  $\mu_{\text{vis}}$  values obtained with the zero-count method using the number of hits in the PU and the track count in the VELO as a function of time in seconds relative to the first run of LHCb in 2010. The period spans the full 2010 data taking period (about half a year). The dashed lines show the average value of the starting and ending periods (the first and last 25 runs, respectively) and differ by  $\approx 1\%$ . The changes in the average values between the three main groups ( $t < 0.4 \times 10^7$  s,  $0.4 \times 10^7 < t < 1.2 \times 10^7$  s,  $t > 1.2 \times 10^7$  s) coincide with known maintenance changes to the PU system. The upward excursion near  $1.05 \times 10^7$  s is due to background introduced by parasitic collisions located at 37.5 m from the nominal IP present in the bunch filling scheme used for these fills to which the two counters have different sensitivity. The downward excursion near  $0.25 \times 10^7$  s is due to known hardware failures in the PU (recovered after maintenance). The statistical errors are smaller than the symbol size of the data points.

25 ns intervals and is used to measure the relative charges of the individual bunches. The DCCT is absolutely calibrated, thus is used to constrain the total number of particles, while the FBCT defines the relative bunch populations. The procedure is described in detail in Ref. [20]. All devices have two independent readout systems. For the DCCT both systems provide reliable information and their average is used in the analysis, while for the FBCT one of the two systems is dedicated to tests and cannot be used.

The absolute calibration of the DCCT is determined using a high-precision current source. At low intensity (early data) the noise in the DCCT readings is relatively important, while at the higher intensities of the data taken in October 2010 this effect is negligible. The noise level and its variation is determined by interpolating the average DCCT readings over long periods of time without beam before and after the relevant fills.

In addition to the absolute calibration of the DCCTs, a deviation from the proportionality of the FBCT readings to the individual bunch charges is a potential source of systematic uncertainty. The FBCT charge offsets are cross checked using the ATLAS BPTX (timing) system [21]. This

comparison shows small discrepancies between their offsets. These deviations are used as an estimate of the uncertainties. Since the FBCT equipment is readjusted at regular intervals, the offsets can vary on a fill-by-fill basis. Following the discussion in Ref. [20], an estimate of 2.9% is used for the uncertainty of an individual bunch population product of a colliding bunch pair. Owing to the DCCT constraint on the total beam current, the overall uncertainty is reduced when averaging results of different bunch pairs within a single fill. As will be discussed in Sect. 5, for the analysis of the VDM data a method can be used which only needs the assumption of the linearity of the FBCT response.

The LHC radio frequency (RF) system operates at 400 MHz, compared to the nominal 40 MHz bunch frequency. If protons circulate in the ring outside the nominal RF buckets, the readings of the DCCT need to be corrected before they are used to normalize the sum of the FBCT signals. We define “satellite” bunches as charges in neighbouring RF buckets compared to the nominal bucket. Satellite bunches inside the nominally filled bunch slots can be detected by the LHC experiments when there is no (or a very small) crossing angle between the two beams. The satellites would be observed as interactions displaced by a multiple of 37.5 cm from the nominal intersection point. For a part of the 2010 run the ATLAS and CMS experiments were operating with zero crossing angle and displaced interactions were indeed observed [20].

The “ghost charge” is defined as the charge outside the nominally filled bunch slots. The rates of beam-gas events produced by “ghost” and nominal protons are measured using the beam-gas trigger. The ghost fraction is determined by comparing the number of beam-gas interactions during ee crossings with the numbers observed in be and eb crossings. The timing of the LHCb trigger is optimized for interactions in the nominal RF buckets. The trigger efficiency depends on the time of the interaction with respect to the phase of the clock (modulo 25 ns). A measurement of the trigger efficiency was performed by shifting the clock which is usually synchronized with the LHC bunch-crossing time by 5, 10 and 12.5 ns and by comparing the total beam-gas rates in the nominal crossings. From these data the average efficiency for ghost charge is obtained to be  $\epsilon_{\text{average}} = 0.86 \pm 0.14$  ( $0.84 \pm 0.16$ ) for beam 1 (beam 2). The ghost charge is measured for each fill during which an absolute luminosity measurement is performed and is typically 1% of the total beam charge or less. The contribution of “ghost” protons to the total LHC beam current is subtracted from the DCCT value before the sum of the FBCT bunch populations is constrained by the DCCT measurement of the total current. The uncertainty assigned to the subtraction of ghost charge varies per fill and is due to the trigger efficiency uncertainty and the limited statistical accuracy. These two error components are of comparable size.

## 5. The van der Meer scan (VDM) method

The beam position scanning method, invented by van der Meer, provides a direct determination of an effective cross-section  $\sigma_{\text{vis}}$  by measuring the corresponding counting rate as a function of the position offsets of two colliding beams [8]. At the ISR only vertical displacements were needed owing to the crossing angle between the beams in the horizontal plane and to the fact that the beams were not bunched. For the LHC the beams have to be scanned in both transverse directions due to the fact that the beams are bunched [9]. The cross-section  $\sigma_{\text{vis}}$  can be measured for two colliding

**Table 1.** Parameters of LHCb van der Meer scans.  $N_{1,2}$  is the typical number of protons per bunch,  $\beta^*$  characterizes the beam optics near the IP,  $n_{\text{tot}}$  ( $n_{\text{coll}}$ ) is the total number of (colliding) bunches per beam,  $\mu_{\text{vis}}^{\text{max}}$  is the average number of visible interactions per crossing at the beam positions with maximal rate.  $\tau_{N_1 N_2}$  is the decay time of the product of the bunch populations and  $\tau_L$  is the decay time of the luminosity.

	25 Apr	15 Oct
LHC fill number	1059	1422
$N_{1,2}$ ( $10^{10}$ protons)	1	7–8
$\beta^*$ (m)	2	3.5
$n_{\text{coll}}/n_{\text{tot}}$	1/2	12/16
$\mu_{\text{vis}}^{\text{max}}$	0.03	1
Trigger	minimum bias	22.5 kHz random $\sim 130$ Hz minimum bias beam-gas
$\tau_{N_1 N_2}$ (h)	950	700
$\tau_L$ (h)	30	46

bunches using the equation [15]

$$\sigma_{\text{vis}} = \frac{\int \mu_{\text{vis}}(\Delta_x, \Delta_{y_0}) d\Delta_x \int \mu_{\text{vis}}(\Delta_{x_0}, \Delta_y) d\Delta_y}{N_1 N_2 \mu_{\text{vis}}(\Delta_{x_0}, \Delta_{y_0}) \cos \alpha}, \quad (5.1)$$

where  $\mu_{\text{vis}}(\Delta_x, \Delta_y)$  is the average number of interactions per crossing at offset  $(\Delta_x, \Delta_y)$  corresponding to the cross-section  $\sigma_{\text{vis}}$ . The interaction rates  $R(\Delta_x, \Delta_y)$  are related to  $\mu_{\text{vis}}(\Delta_x, \Delta_y)$  by the revolution frequency,  $R(\Delta_x, \Delta_y) = f \mu_{\text{vis}}(\Delta_x, \Delta_y)$ . These rates are measured at offsets  $\Delta_x$  and  $\Delta_y$  with respect to their nominal positions at offsets  $(\Delta_{x_0}, \Delta_{y_0})$ . The scans consist of creating offsets  $\Delta_x$  and  $\Delta_y$  such that practically the full profiles of the beams are explored. The measured rate integrated over the displacements gives the cross-section.

The main assumption is that the density distributions in the orthogonal coordinates  $x$  and  $y$  can be factorized. In that case, two scans are sufficient to obtain the cross-section: one along a constant  $y$ -displacement  $\Delta_{y_0}$  and one along a constant  $x$ -displacement  $\Delta_{x_0}$ . It is also assumed that effects due to bunch evolution during the scans (shape distortions or transverse kicks due to beam-beam effects, emittance growth, bunch current decay), effects due to the tails of the bunch density distribution in the transverse plane and effects of the absolute length scale calibration against magnet current trims are either negligible or can be corrected for.

## 5.1 Experimental conditions during the van der Meer scan

VDM scans were performed in LHCb during dedicated LHC fills at the beginning and at the end of the 2010 running period, one in April and one in October. The characteristics of the beams are summarized in Table 1. In both fills there is one scan where both beams moved symmetrically and one scan where only one beam moved at a time. Precise beam positions are calculated from the LHC magnet currents and cross checked with vertex measurements using the LHCb VELO, as described below.

In April the maximal beam movement of  $\pm 3\sigma$  was achieved only in the first scan, as in the second only the first beam was allowed to move.<sup>3</sup> During the second October scan, both beams moved one after the other, covering the whole separation range of  $\approx 6\sigma$  to both sides. However, the beam steering procedure was such that in the middle of the scan the first beam jumped to an opposite end point and then returned, so that the beam movement was not continuous. This potentially increases hysteresis effects in the LHC magnets. In addition, the second scan in October had half the data points, so it was used only as a cross check to estimate systematic errors.

During the April scans the event rate was low and it was possible to record all events containing visible interactions. A loose minimum bias trigger was used with minimal requirements on the number of SPD hits ( $\geq 3$ ) and the transverse energy deposition in the calorimeters ( $\geq 240$  MeV). In October the bunch populations were higher by a factor  $\sim 7.5$ , therefore, in spite of slightly broader beams (the optics defined a  $\beta^*$  value of 3.5 m instead of 2 m in April), the rate per colliding bunch pair was higher by a factor of  $\sim 30$ . There were twelve colliding bunch pairs instead of one in April. Therefore, a selective trigger was used composed of the logical OR of three independent criteria. The first decision accepted random bunch crossings at 22.5 kHz (20 kHz were devoted to the twelve crossings with collisions, 2 kHz to the crossings where only one of two beams was present, and 0.5 kHz to the empty crossings). The second decision used the same loose minimum bias trigger as the one used in April but its rate was limited to 130 Hz. The third decision collected events for the beam-gas analysis.

For both the April and October data the systematic error is dominated by uncertainties in the bunch populations. In April this uncertainty is higher (5.6%) due to a larger contribution from the offset uncertainty at lower bunch populations [20]. In October the measurement of the bunch populations was more precise, but its uncertainty (2.7%) is still dominant in the cross-section determination [22]. Since the dominant uncertainties are systematic and correlated between the two scans, we use the less precise April scan only as a cross check. The scans give consistent results, and in the following we concentrate on the scan taken in October which gives about a factor two better overall precision in the measurement.

The LHC filling scheme was chosen in such a way that all bunches collided only in one experiment (except for ATLAS and CMS where the bunches are always shared), namely twelve bunch pairs in LHCb, three in ATLAS/CMS and one in ALICE. The populations of the bunches colliding in LHCb changed during the two LHCb scans by less than 0.1%. Therefore, the rates are not normalized by the bunch population product  $N_1 N_2$  of each colliding bunch pair at every scan point, but instead only the average of the product over the scan duration is used. This is done to avoid the noise associated with the  $N_{1,2}$  measurement. The averaged bunch populations are given in Table 2. The same procedure is applied for the April scan, when the decay time of  $N_1 N_2$  was longer, 950 instead of 700 hours in October.

In addition to the bunch population changes, the luminosity stability may be limited by the changes in the bunch profiles, *e.g.* by emittance growth. The luminosity stability is checked several times during the scans when the beams were brought back to their nominal position. The average number of interactions per crossing is shown in Fig. 4 for the October scan. The luminosity decay time is measured to be 46 hours (30 hours in April). This corresponds to a 0.7% luminosity drop

---

<sup>3</sup>We refer here to  $1\sigma$  as the average of the approximate widths of the beams.



**Table 2.** Bunch populations (in  $10^{10}$  particles) averaged over the two scan periods in October separately. The bottom line is the DCCT measurement, all other values are given by the FBCT. The first 12 rows are the measurements in bunch crossings (BX) with collisions at LHCb, and the last two lines are the sums over all 16 bunches.

BX	Scan 1		Scan 2	
	$N_1$	$N_2$	$N_1$	$N_2$
2027	8.425	7.954	8.421	7.951
2077	7.949	7.959	7.944	7.957
2127	7.457	7.563	7.452	7.561
2177	6.589	7.024	6.584	7.021
2237	7.315	8.257	7.311	8.255
2287	7.451	7.280	7.446	7.278
2337	7.016	7.219	7.012	7.217
2387	7.803	6.808	7.798	6.805
2447	7.585	7.744	7.580	7.742
2497	7.878	7.747	7.874	7.745
2547	6.960	6.244	6.955	6.243
2597	7.476	7.411	7.472	7.409
All, FBCT	120.32	119.07	120.18	118.99
DCCT	120.26	119.08	120.10	118.98

during the first, longer, scan along either  $\Delta_x$  or  $\Delta_y$  (0.9% in April). The scan points have been taken from lower to higher  $\Delta_x$ ,  $\Delta_y$  values, therefore, the luminosity drop effectively enhances the left part of the integral and reduces its right part, so that the net effect cancels to first order since the curve is symmetric. The count rate  $R(\Delta_{x0}, \Delta_{y0})$  at the nominal position entering Eq. 5.1, is measured in the beginning, in the middle and at the end of every scan, so that the luminosity drop also cancels to first order. Therefore, the systematic error due to the luminosity drop is much less than 0.7% and is neglected.

The widths of the profiles of the luminous region did not change within the statistical uncertainties when the beams were brought to their nominal positions during the first and the second scans in  $\Delta_x$  and  $\Delta_y$ . In addition, the width of the profiles measured in the two VDM scans did not change. These facts also indicate that the effect of the emittance growth on the cross-section measurement is negligible.

## 5.2 Cross-section determination

In accordance with the definition of the most stable relative luminosity counter, a visible event is defined as a  $pp$  interaction with at least two VELO tracks. The twelve colliding bunch pairs of the VDM scan in October are analysed individually. The dependence on the separation  $\Delta_x$  and  $\Delta_y$  of  $\mu_{\text{vis}}$  summed over all bunches is shown in Fig. 5. Two scans are overlaid, the second is taken at the same values of  $\Delta_x$  and  $\Delta_y$  but with twice as large a step size and different absolute beam positions. One can see that the  $\Delta_y$  curves are not well reproduced in the two scans. The reason for this apparent non-reproducibility is not understood. It may be attributed to hysteresis effects or

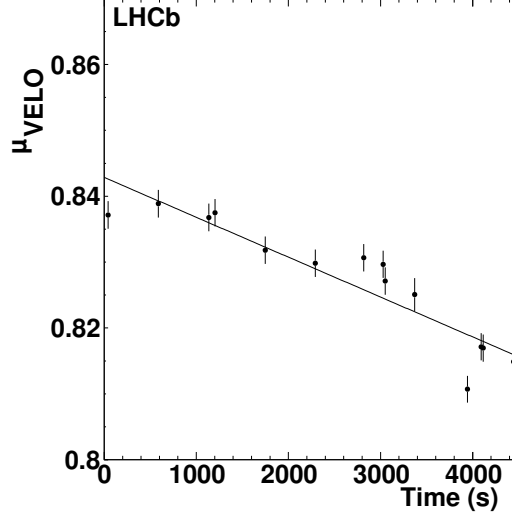


**Figure 4.** Evolution of the average number of interactions per crossing at the nominal beam position during the October scans. In the first (second) scan the parameters at the nominal beam position were measured three (four) times both during the  $\Delta_x$  scan and the  $\Delta_y$  scan. The straight line is a fit to the data. The luminosity decay time is 46 hours.

**Table 3.** Mean and RMS of the VDM count-rate profiles summed over the twelve colliding bunch pairs obtained from data in the two October scans (scan 1 and scan 2). The statistical errors are  $0.05 \mu\text{m}$  in the mean position and  $0.04 \mu\text{m}$  in the RMS.

	Scan	$\Delta_x$ scan	$\Delta_y$ scan
Mean ( $\mu\text{m}$ )	1	1.3	3.1
	2	2.8	9.2
RMS ( $\mu\text{m}$ )	1	80.6	80.8
	2	80.5	80.7

imperfections in the description of the optics.<sup>4</sup>

The mean and RMS values of the VDM count-rate profiles shown in Fig. 5 are listed in Table 3. Single Gaussian fits to the individual bunch profiles return  $\chi^2$  values between 2.7 and 4.3 per degree of freedom. Double Gaussian fits provide a much better description of the data and are therefore used in the analysis. The single Gaussian fits give cross-section values typically 1.5 to 2% larger than the ones obtained with a double Gaussian. It is found that the fit errors can be reduced by approximately a factor two if the fits to the  $\Delta_x$  and  $\Delta_y$  curves are performed simultaneously and the value measured at the nominal point  $\mu_{\text{vis}}(\Delta_{x_0}, \Delta_{y_0})$  is constrained to be the same in both scans. The first fit parameter is chosen to be  $\int \mu_{\text{vis}} d\Delta_x \int \mu_{\text{vis}} d\Delta_y / \mu_{\text{vis}}(\Delta_{x_0}, \Delta_{y_0})$ , so that a correlation of both integrals and the value at the nominal point is correctly taken into account in the resulting fit error. Other fit parameters are: the two integrals along  $\Delta_x$  and  $\Delta_y$ , and  $\sigma_1$ ,  $\Delta\sigma$  and a common central position of the Gaussian function for the  $\Delta_x$  and similarly for the  $\Delta_y$  curves. Here  $\sigma_1$  and

<sup>4</sup>Imperfections in the description of the optics can manifest themselves as second order effects in the translation of magnet settings into beam positions or beam angles.

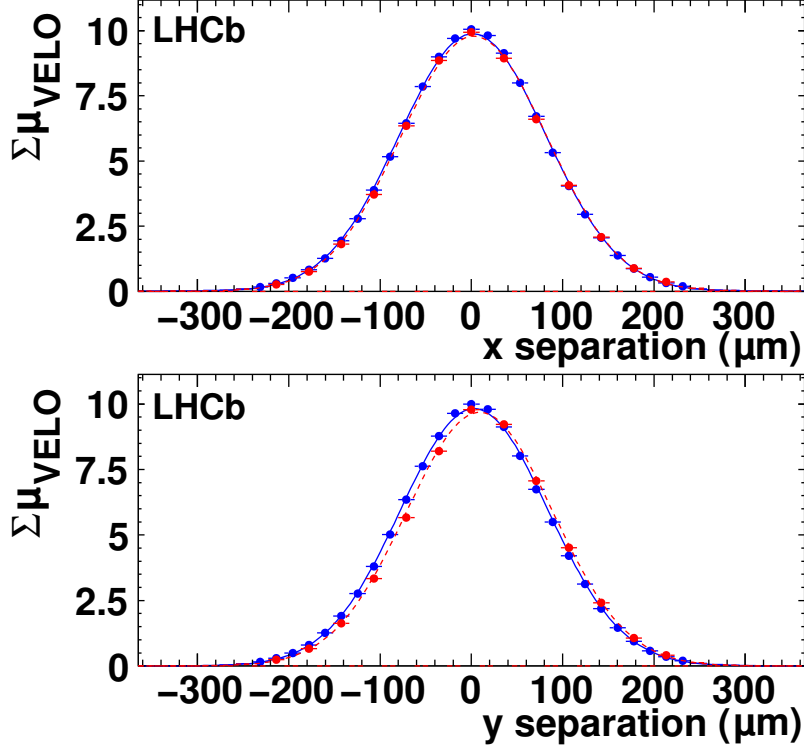


**Figure 5.** Number of interactions per crossing summed over the twelve colliding bunches versus the separations  $\Delta_x$  (top),  $\Delta_y$  (bottom) in October. The first (second) scan is represented by the dark/blue (shaded/red) points and the solid (dashed) lines. The spread of the mean values and widths of the distributions obtained individually for each colliding pair are small compared to the widths of the VDM profiles, so that the sum gives a good illustration of the shape. The curves represent the single Gaussian fits to the data points described in the text.

$\sigma_2 = \sqrt{\sigma_1^2 + \Delta\sigma^2}$  are the two Gaussian widths of the fit function. The relative normalization of the two Gaussian components and the value at the nominal point are derived from the nine fit parameters listed above. The  $\chi^2$  value per degree of freedom of the fit is between 0.7 and 1.8 for all bunch pairs.

The product of bunch populations  $N_1 N_2$  of the twelve colliding bunches have an RMS spread of 12%. The analysis of the individual bunch pairs gives cross-sections consistent within statistical errors, which typically have values of 0.29% in the first scan. The sensitivity of the method is high enough that it is possible to calibrate the *relative* bunch populations  $N_{1,2}^i / \sum_{j=1}^{16} N_{1,2}^j$  measured with the FBCT system by assuming a linear response. Here  $i$  runs over the twelve bunches colliding in LHCb and  $j$  over all 16 bunches circulating in the machine. By comparing the FBCT with the ATLAS BPTX measurements it is observed that both may have a non-zero offset [20, 22]. A discrete function  $s_{\text{vis}}^i$  is fitted to the twelve measurements  $\sigma_{\text{vis}}^i$  using three free parameters: the common cross-section  $\sigma_{\text{vis}}$  and the two FBCT offsets for the two beams  $N_{1,2}^0$

$$s_{\text{vis}}^i = \sigma_{\text{vis}} \prod_{b=1,2} \left[ \frac{(N_b^i - N_b^0)}{N_b^i} \frac{\sum_{j=1}^{16} N_b^j}{\sum_{j=1}^{16} (N_b^j - N_b^0)} \right], \quad (5.2)$$

**Table 4.** Results for the visible cross-section fitted over the twelve bunches colliding in LHCb for the October VDM data together with the results of the April scans.  $N_{1,2}^0$  are the FBCT or BPTX offsets in units of  $10^{10}$  particles. They should be subtracted from the values measured for individual bunches. The first (last) two columns give the results for the first and the second scan using the FBCT (BPTX) to measure the relative bunch populations. The cross-section from the first scan obtained with the FBCT bunch populations with offsets determined by the fit is used as final VDM luminosity calibration. The results of the April scans are reported on the last row. Since there is only one colliding bunch pair, no fit to the FBCT offsets is possible.

<b>October data</b>				
	<b>FBCT</b>		<b>ATLAS BPTX</b>	
	<b>Scan 1</b>	<b>Scan 2</b>	<b>Scan 1</b>	<b>Scan 2</b>
	<i>with fitted offsets</i>		<i>with fitted offsets</i>	
$\sigma_{\text{vis}}$ (mb)	<b><math>58.73 \pm 0.05</math></b>	$57.50 \pm 0.07$	$58.62 \pm 0.05$	$57.45 \pm 0.07$
$N_1^0$	$0.40 \pm 0.10$	$0.29 \pm 0.15$	$-0.10 \pm 0.12$	$-0.23 \pm 0.17$
$N_2^0$	$-0.02 \pm 0.10$	$0.23 \pm 0.13$	$-0.63 \pm 0.12$	$-0.34 \pm 0.15$
$\chi^2/\text{ndf}$	$5.8 / 9$	$7.6 / 9$	$6.9 / 9$	$7.3 / 9$
	<i>with offsets fixed at zero</i>		<i>with offsets fixed at zero</i>	
$\sigma_{\text{vis}}$ (mb)	$58.73 \pm 0.05$	$57.50 \pm 0.07$	$58.63 \pm 0.05$	$57.46 \pm 0.07$
$\chi^2/\text{ndf}$	$23.5 / 11$	$21.9 / 11$	$66.5 / 11$	$23.5 / 11$
<b>April data</b>				
	<b>Scan 1</b>	<b>Scan 2</b>		
$\sigma_{\text{vis}}$ (mb)	$59.6 \pm 0.5$	$57.0 \pm 0.5$		

which corrects the relative populations  $N_{1,2}^i$  for the FBCT offsets  $N_{1,2}^0$  and takes into account that the total beam intensities measured with the DCCT constrain the sums of all bunch populations obtained from the FBCT values. The sum over all bunches of the quantities  $N_{1,2}^j$ ,  $\sum_{j=1}^{16} N_{1,2}^j$ , is normalized to the DCCT value prior to the fit and the fit using Eq. 5.2 evaluates the correction due to the FBCT offsets alone. The results of this fit are shown in Fig. 6, where the data points  $\sigma_{\text{vis}}^i$  are drawn without offset correction and the lines represent the fit function of Eq. 5.2. The use of two offsets improves the description of the points compared to the uncorrected simple fit. The  $\chi^2$  per degree of freedom and other relevant fit results are summarized in Table 4. In addition, the table also shows results for the case where the ATLAS BPTX is used instead of the FBCT system.

One can see that the offset errors in the first scan are  $(0.10 - 0.12) \times 10^{10}$ , or 1.5% relative to the average bunch population  $\langle N_{1,2} \rangle = 7.5 \times 10^{10}$ . The sensitivity of the method, therefore, is very high, in spite of the fact that the RMS spread of the bunch population products  $N_1 N_2$  is 12%. The quoted errors are only statistical. For the first scan, the relative cross-section error is 0.09%. Since the fits return good  $\chi^2$  values, the bunch-crossing dependent systematic uncertainties (such as emittance growth and bunch population product drop) are expected to be lower or comparable. An indication of the level of the systematic errors is given by the difference of about two standard deviations found for  $N_{1,2}^0$  between the two scans. All principal sources of systematic errors which will be discussed below (DCCT scale uncertainty, hysteresis, and ghost charges) cancel when comparing bunches within a single scan.

In spite of the good agreement between the bunches within the same scan, there is an overall

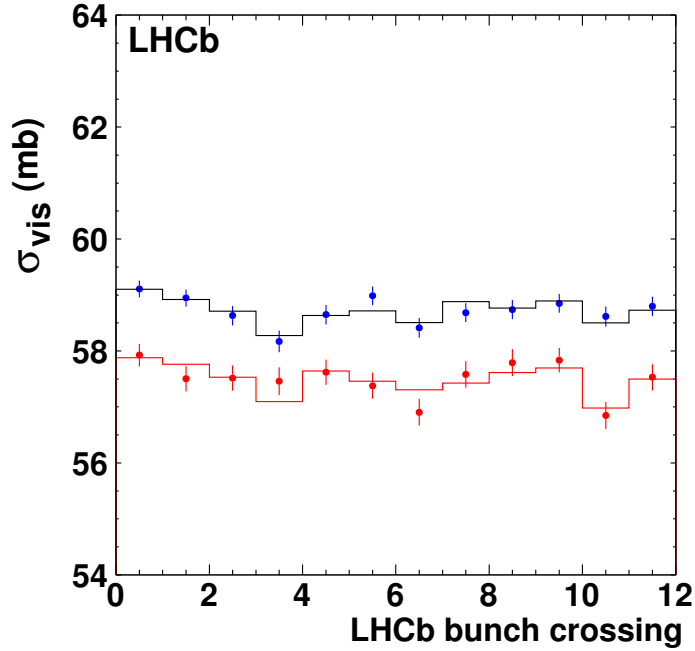


**Figure 6.** Cross-sections without correction for the FBCT offset for the twelve bunches of the October VDM fill (data points). The lines indicate the results of the fit as discussed in the text. The upper (lower) set of points is obtained in the first (second) scan.

2.1% discrepancy between the scans. The reason is not understood, and may be attributed to a potential hysteresis effect or similar effects resulting in uncontrollable shifts of the beam as a whole. The results of the first scan with the FBCT offsets determined by the fit are taken as the final VDM luminosity determination (see Sect. 5.4). The 2.1% uncertainty estimated from the discrepancy is the second largest systematic error in the cross-section measurement after the uncertainties in the bunch populations. In the April data the situation is similar: the discrepancy between the cross-sections obtained from the two scans is  $(4.4 \pm 1.2)\%$ , the results may be found in Table 4. Since the April measurement is performed using corrected trigger rates proportional to the luminosity instead of VELO tracks, the results have been corrected for the difference in acceptances. The correction factor is determined by studying random triggers and is  $\sigma_{\text{VELO}}/\sigma_{\text{April trigger}} = 1.066$ , where  $\sigma_{\text{VELO}}$  is the usual definition of  $\sigma_{\text{vis}}$ .

### 5.3 Systematic errors

#### 5.3.1 Reproducibility of the luminosity at the nominal beam positions

Figure 4 shows the evolution of the luminosity as a function of time for the periods where the beams were at their nominal positions during the VDM scan. One expects a behaviour which follows the loss of beam particles and the emittance growth. Since these effects occur at large time-scales compared to the duration of the scan, the dependence on these known effects can be approximated by a linear evolution. As shown in Fig. 4, the luminosity did not always return to the expected value when the beams returned to their nominal positions. The  $\chi^2/\text{ndf}$  with respect to the fitted straight line is too large (40/12), thus, the non-reproducibility cannot be attributed

fully to statistical fluctuations and another systematic effect is present. The origin of this effect is not understood but it may be similar to the one which causes the non-reproducibility of the beam positions observed in the shift of the two scan curves. Therefore, a systematic error of 0.4% is assigned to the absolute scale of the  $\mu_{\text{vis}}$  measurement to take this observation into account. The systematic error is estimated as the amount which should be added in quadrature to the statistical error of 0.25% to produce a  $\chi^2/\text{ndf}$  equal to one. Since the absolute scale of the  $\mu_{\text{vis}}$  measurement enters the cross-section linearly (Eq. 5.1), the same systematic error of 0.4% is assigned to the cross-section measurement.

### 5.3.2 Length scale calibration

The beam separation values  $\Delta_x$  and  $\Delta_y$  are calculated from the LHC magnet currents at every scan step. There is a small non-reproducibility in the results of two scans, as shown in Fig. 5. The non-reproducibility may be attributed to a mismatch between the actual beam positions and the nominal ones. Therefore, it is important to check the  $\Delta_x$  and  $\Delta_y$  values as predicted by the magnet currents, and in particular their scales which enter linearly in the cross-section computation (Eq. 5.1). One distinguishes a possible differential length scale mismatch between the two beams from a mismatch of their average position calibration.

A dedicated mini-scan was performed in October where the two beams were moved in five equidistant steps both in  $x$  and  $y$  keeping the nominal separation between the beams constant. During the scan along  $x$  the beam separation was 80  $\mu\text{m}$  in  $x$  and 0  $\mu\text{m}$  in  $y$ . Here 80  $\mu\text{m}$  is approximately the width of the luminosity profile of the VDM scan (see Table 3). This separation was chosen to maximize the derivative  $dL/d\Delta(x)$ , *i.e.* the sensitivity of the luminosity to a possible difference in the length scales for the two beams. If *e.g.* the first beam moves slightly faster than the second one compared to the nominal movement, the separation  $\Delta(x)$  gets smaller and the effect can be visible as an increase of the luminosity. Similarly, the beam separation used in the  $y$  scan was 0  $\mu\text{m}$  and 80  $\mu\text{m}$  in  $x$  and  $y$ , respectively.

The behaviour of the measured luminosity during the length-scale calibration scans is shown in Fig. 7. As one can see, the points show a significant deviation from a constant. This effect may be attributed to different length scales of the two beams. More specifically, we assume that the real positions of the beams  $x_{1,2}$  could be obtained from the values  $x_{1,2}^0$  derived from the LHC magnet currents by applying a correction parametrized by  $\varepsilon_x$

$$x_{1,2} = (1 \pm \varepsilon_x/2)x_{1,2}^0, \quad (5.3)$$

and similarly for  $y_{1,2}$ . The  $+$  ( $-$ ) sign in front of  $\varepsilon_x$  holds for beam 1 (beam 2). Assuming a Gaussian shape of the luminosity dependence on  $\Delta_x$  during the VDM scan, we get

$$\frac{1}{L} \frac{dL}{d(x_1 + x_2)/2} = -\varepsilon_x \frac{\Delta_x}{\Sigma_x^2}. \quad (5.4)$$

Here  $\Delta_x = 80 \mu\text{m}$  is the fixed nominal beam separation. A similar equation holds for the  $y$  coordinate. In the approximation of a single Gaussian shape of the beams, the width of the VDM profile,  $\Sigma_x$ , is defined as

$$\Sigma_x = \sqrt{\sigma_{1x}^2 + \sigma_{2x}^2 + 4(\sigma_{\otimes z})^2 \tan^2 \alpha}, \quad (5.5)$$

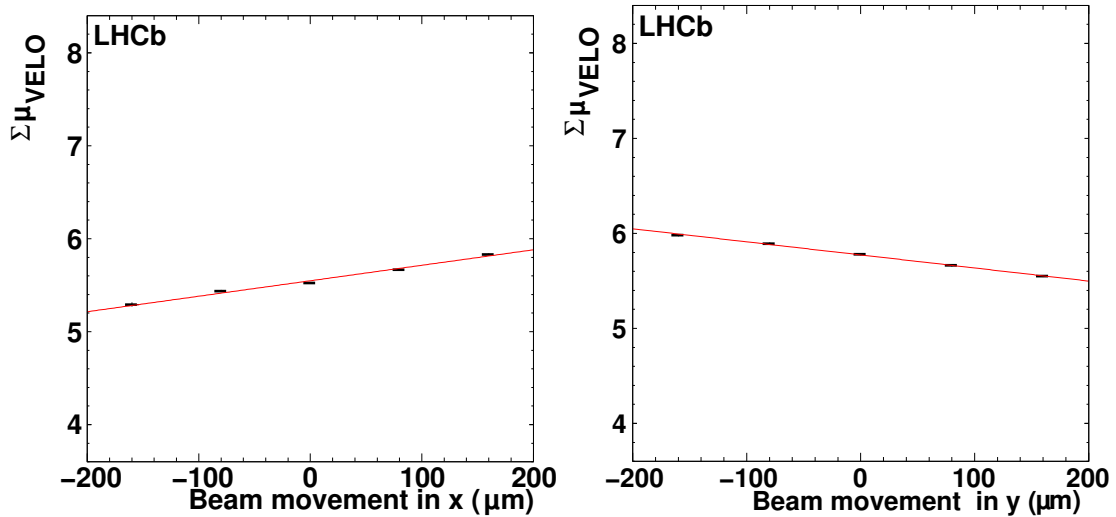


**Figure 7.** Average number of interactions ( $\mu_{\text{VELO}}$ ) versus the centre of the luminous region summed over the twelve colliding bunches and measured during the length scale scans in  $x$  (left) and in  $y$  (right) taken in October. The points are indicated with small horizontal bars, the statistical errors are smaller than the symbol size. The straight-line fit is overlaid.

where  $\sigma_{\otimes z}$  is the width of the luminous region in the  $z$  coordinate and  $\sigma_{bx}$  is the width of beam  $b$  ( $b = 1, 2$ ). A similar equation can be written for  $\Sigma_y$ . From the slopes observed in Fig. 7 we obtain  $\epsilon_x = 2.4\%$  and  $\epsilon_y = -1.9\%$ . The same behaviour is observed for all bunches separately.

Since  $\Delta_x = (x_1^0 - x_2^0) + \epsilon(x_1^0 + x_2^0)/2$ , the  $\Delta_x$  correction depends on the nominal mid-point between the beams  $(x_1^0 + x_2^0)/2$ . In the first scan this nominal point was always kept at zero, therefore, no correction is needed. During the second scan this point moved with nominal positions  $0 \rightarrow 355.9 \mu\text{m} \rightarrow 0$ . Therefore, a correction to the  $\Delta_x$  values in Fig. 5 is required. The central point should be shifted to the right (left) for the  $x$  ( $y$ ) scan. The left (right) side is thus stretched and the opposite side is shrunk. After correction the shift between the scans is reduced in  $y$ , but appears now in  $x$ , so that the discrepancy cannot be fully explained by a linear correction alone. The correction which stretches or shrinks the profiles measured in the second scan influences the integrals of these profiles and the resulting cross-sections very little. The latter changes on average by only 0.1%, which we take as an uncertainty and which we include into the systematic error. In Table 4 the numbers are given with the correction applied.

During a simultaneous parallel translation of both beams, the centre of the luminous region should follow the beam positions regardless of the bunch shapes. Since it is approximately at  $(x_1 + x_2)/2 = (x_1^0 + x_2^0)/2$  and similarly for  $y$ , the corrections to the position of the centre due to  $\epsilon_{x,y}$  are negligible. The luminous centre can be determined using vertices measured with the VELO. This provides a precise cross check of the common beam length scales  $(x_1^0 + x_2^0)/2$  and  $(y_1^0 + y_2^0)/2$ . The result is shown in Fig. 8. The LHC and VELO length scales agree within  $(-0.97 \pm 0.17)\%$  and  $(-0.33 \pm 0.15)\%$  in  $x$  and  $y$ , respectively. The scale of the transverse position measurement with the VELO is expected to be very precise owing to the fact that it is determined by the strip positions of the silicon sensors with a well-known geometry. For the cross-section determination we took the more precise VELO length scale and multiplied the values from Table 4 by

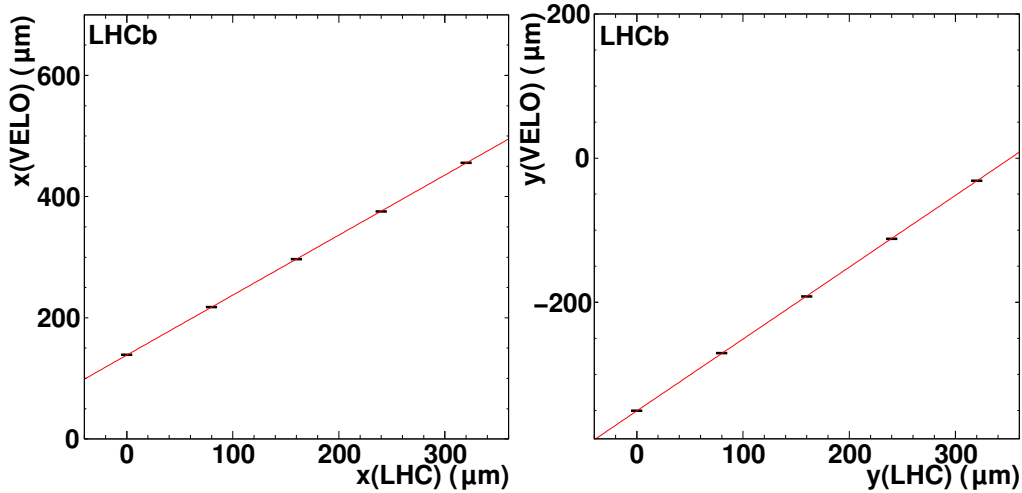


**Figure 8.** Centre of the luminous region reconstructed with VELO tracks versus the position predicted by the LHC magnet currents. The points are indicated with small horizontal bars, the statistical errors are smaller than the symbol size. The points are fitted to a linear function. The slope calibrates the common length scale.

$(1 - 0.0097) \times (1 - 0.0033) = 0.9870$ . In addition, we conservatively assigned a 1% systematic error due to the common scale uncertainty.

In April, no dedicated length scale calibration was performed. However, a cross check is available from the distance between the centre of the luminous region measured with the VELO and the nominal centre position. The comparison of these distances between the first and second scan when either both beams moved symmetrically or only the first beam moved, provides a cross check which does not depend on the bunch shapes. From this observation the differences of the length scales between the nominal beam movements and the VELO reference are found to be  $(-1.3 \pm 0.9)\%$  and  $(1.5 \pm 0.9)\%$  for  $\Delta_x$  and  $\Delta_y$ , respectively. Conservatively a 2% systematic error is assigned to the length scale calibration for the scans taken in April.

### 5.3.3 Coupling between the $x$ and $y$ coordinates in the LHC beams

The LHC ring is tilted with respect to the horizontal plane, while the VELO detector is aligned with respect to a coordinate system where the  $x$  axis is in a horizontal plane [23]. The van der Meer equation (Eq. 5.1) is valid only if the particle distributions in  $x$  and in  $y$  are independent. To check this condition the movement of the centre of the luminous region along  $y$  is measured during the length scale scan in  $x$  and vice versa. This movement is compatible with the expected tilt of the LHC ring of 13 mrad at LHCb [23] with respect to the vertical and the horizontal axes of the VELO. The corresponding correction to the cross-section is negligible ( $< 10^{-3}$ ).

To measure a possible  $x$ - $y$  correlation in the machine the two-dimensional vertex map is studied by determining the centre position in one coordinate for different values of the other coordinate. For the analysis, data were collected with the beams colliding head-on at LHCb in Fill 1422, during which also the VDM scan data were taken. Figure 9 shows the  $x$ - $y$  profile of the luminous region. The centre positions of the  $y$  coordinate lie on a straight line with a slope of 79 mrad. The slopes found in the corresponding  $x$ - $z$  and  $y$ - $z$  profiles are  $-92 \mu\text{rad}$  and  $44 \mu\text{rad}$ . These slopes are due



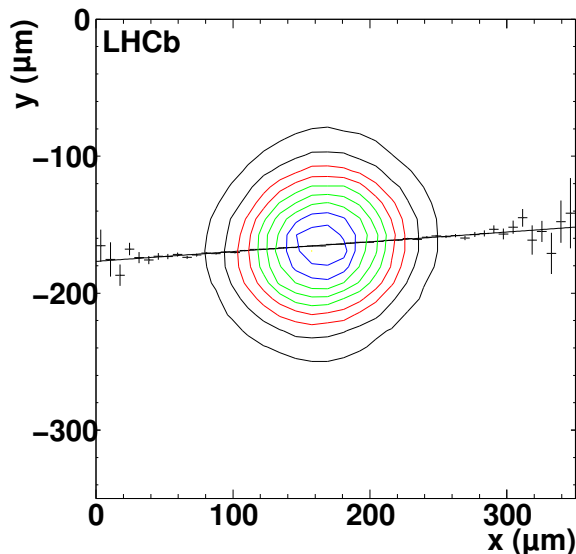


**Figure 9.** Contours of the distribution of the  $x$ - $y$  coordinates of the luminous region. The contour lines show the values at multiples of 10% of the maximum. The points represent the  $y$ -coordinates of the centre of the luminous region in different  $x$  slices. They are fitted with a linear function.

to the known fact that the middle line between the two LHC beams is inclined with respect to the  $z$  axis. This is observed with beam gas events, the inclination varies slightly from fill to fill. The measurement of the beam directions will be described in detail in Sect. 6. Taking into account these known correlations of  $x$  and  $y$  with  $z$  and also the known 13 mrad tilt of the LHC ring, one can calculate the residual slope of the  $x$ - $y$  correlation, which is predicted to be 77 mrad.

If the beam profiles are two-dimensional Gaussian functions with a non-zero correlation between the  $x$  and  $y$  coordinates, the cross-section relation (Eq. 5.1) should be corrected. We assume that the  $x$ - $y$  correlation coefficients of the two beams,  $\zeta$ , are similar and, therefore, close to the measured correlation in the distribution of the vertex coordinates of the luminous region,  $\zeta = 0.077$ . In this case the correction to the cross-section is  $\zeta^2/2 = 0.3\%$ . We do not apply a corresponding correction, but instead include 0.3% uncertainty as an additional systematic error.

### 5.3.4 Cross check with the $z$ position of the luminous region

A cross check of the width of the luminosity profile as a function of  $\Delta_x$  is made by measuring the movement of the  $z$  position of the centre of the luminous region during the first VDM scan in the  $x$  coordinate in October (see Fig. 10). Assuming Gaussian bunch density distributions and identical widths of the two colliding beams, the slope is equal to

$$\frac{dz_{\otimes}}{d(\Delta_x)} = -\frac{\sin 2\alpha}{4} \frac{\sigma_z^2 - \sigma_x^2}{\sigma_x^2 \cos^2 \alpha + \sigma_z^2 \sin^2 \alpha}, \quad (5.6)$$

where  $\sigma_{x,z}$  are the beam widths in the corresponding directions and  $dz_{\otimes}$  is the induced shift in the  $z$ -coordinate of the centre of the luminous region. We approximate  $\sigma_z$  as  $\sqrt{2}\sigma_{\otimes z}$ . Using the slope observed in Fig. 10 one gets the expected width of the luminosity profile versus  $\Delta_x$ ,  $\sigma_x^{\text{VDM}} = \sqrt{2}\sigma_x = 78 \mu\text{m}$ , in agreement with the measured value of  $80 \mu\text{m}$ . A further cross check is described in Sect. 7.

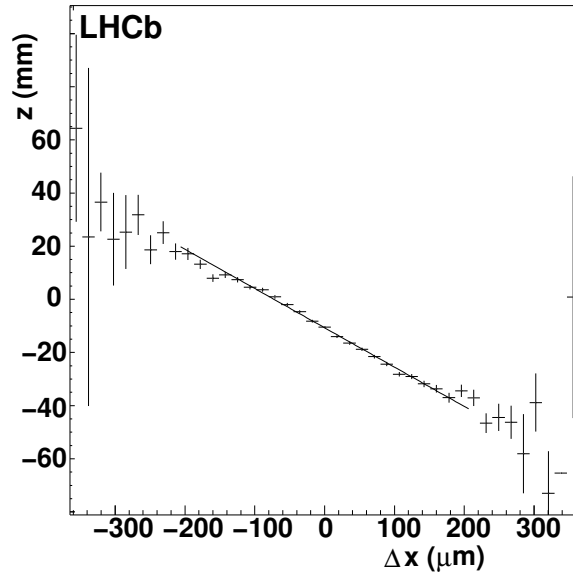


**Figure 10.** Movement of the centre of the luminous region in  $z$  during the first scan in  $x$  taken in October.

**Table 5.** Cross-section of  $pp$  interactions producing at least two VELO tracks, measured in the two van der Meer scans in April and in October.

	$\sigma_{\text{vis}}$ (mb)	Relative uncertainty (%)
April	59.7	7.5
October	<b>58.35</b>	3.64

#### 5.4 Results of the van der Meer scans

The cross-section results obtained with the VDM scans are given in Table 5. We recall that the effective cross-section defined by interactions with at least two VELO tracks is used in the analysis. The results of the two measurement periods are consistent. During the second scan in October the beam movements were not continuous, so the results might suffer from hysteresis effects. In the second scan in April only one beam moved limiting the separation range. Therefore, only the first scans are shown in Table 5 for April and October. Both in the April and in the October measurements the difference observed in the results of the two scans is included as a systematic error. The complete list of errors taken into account is given in Table 6. The uncertainties are uncorrelated and therefore added in quadrature. As already anticipated in Sect. 5.1 the first scan taken in October is retained as the final result of the VDM method since it has much reduced systematic errors compared to the April scans.

## 6. The beam-gas imaging (BGI) method

Tracks measured in the LHCb detector allow vertices from the interactions of beam particles with the residual gas in the machine (beam-gas interactions) and from the beam-beam collisions to be reconstructed. The beam-gas imaging method is based on the measurement of the distributions of these vertices to obtain an image of the transverse bunch profile along the beam trajectory.

**Table 6.** Summary of relative cross-section uncertainties for the van der Meer scans in October and April. Due to the lower precision in the April data some systematic errors could not be evaluated and are indicated with “–”.

Source	relative uncertainty (%)	
	October	April
Relative normalization stability	0.5	0.5
DCCT scale	2.7	2.7
DCCT baseline noise	negligible	3.9
FBCT systematics	0.2	2.9
Ghost charge	0.2	0.1
Statistical error	0.1	0.9
$N_1 N_2$ drop	negligible	negligible
Emittance growth	negligible	negligible
Reproducibility at nominal position	0.4	–
Difference between two scans	2.1	4.4
Average beam length scale	1.0	2.0
Beam length scale difference	0.1	–
Coupling of $x$ and $y$ coordinates	0.3	–
Total	3.6	7.5

This allows the beam angles, profiles and relative positions to be determined. The residual gas in the beam vacuum pipe consists mainly of relatively light elements such as hydrogen, carbon and oxygen.

An important prerequisite for the proper reconstruction of the bunch profiles is the transverse homogeneity of the visualizing gas (see Sect. 6.5.4). A dedicated test performed in October 2010 measured the beam-gas interaction rates as function of beam displacement in a plane perpendicular to the beam axis. The correction to the beam overlap integral due to a possible non-uniform transverse distribution of the residual gas is found to be smaller than 0.05% and is neglected.

Compared to the VDM method, the disadvantage of a small rate is balanced by the advantage that the method is non-disruptive, without beam movements. This means that possible beam-beam effects are constant and effects which depend on the beam displacement, like hysteresis, are avoided. Furthermore, the beam-gas imaging method is applicable during physics fills.

The half crossing-angle  $\alpha$  is small enough to justify setting  $\cos^2 \alpha = 1$  in Eq. 1.1. In the approximation of a vanishing correlation between the transverse coordinates the  $x$  and  $y$  projections can be factorized. At the level of precision required, the bunch shapes are well described by Gaussian distributions. Thus, their shapes are characterized in the  $x$ - $y$  plane at the time of crossing by their widths  $\sigma_{bi}$ , their mean positions  $\xi_{bi}$  ( $i = x, y$ ), and by their bunch length  $\sigma_{bz}$ . The index  $b$  takes the values 1 and 2 according to the two beams. With these approximations, Eq. (1.1) for a single pair of colliding bunches reduces to [24]

$$L = \frac{N_1 N_2 f}{2\pi \sqrt{1 + \tan^2 \alpha (\sigma_{1z}^2 + \sigma_{2z}^2) / (\sigma_{1x}^2 + \sigma_{2x}^2)}} \prod_{i=x,y} \frac{1}{\sqrt{\sigma_{1i}^2 + \sigma_{2i}^2}} \exp\left(-\frac{1}{2} \frac{(\xi_{1i} - \xi_{2i})^2}{\sigma_{1i}^2 + \sigma_{2i}^2}\right), \quad (6.1)$$

where the denominator of the first factor in the product corrects for the crossing angle. The analysis is applied for each individual colliding bunch pair, *i.e.* bunch populations, event rates and beam profiles are considered per bunch pair. Thus, each colliding bunch pair provides an internally consistent measurement of the same visible cross-section. The observables  $\sigma_{bi}$  and  $\xi_{bi}$  are extracted from the transverse distributions of the beam-gas vertices reconstructed in the bb crossings of the colliding bunch pairs (see Sect. 6.2).

The beam overlap-integral is then calculated from the two individual bunch profiles. The simultaneous imaging of the  $pp$  luminous region further constrains the beam parameters. The distribution of  $pp$ -collision vertices, produced by the colliding bunch pair and identified by requiring  $-150 < z < 150$  mm, is used to measure the parameters of the luminous region. Its positions  $\xi_{\otimes i}$  and transverse widths  $\sigma_{\otimes i}$ ,

$$\xi_{\otimes i} = \frac{\xi_{1i}\sigma_{2i}^2 + \xi_{2i}\sigma_{1i}^2}{\sigma_{1i}^2 + \sigma_{2i}^2} \quad \text{and} \quad \sigma_{\otimes i}^2 = \frac{\sigma_{1i}^2\sigma_{2i}^2}{\sigma_{1i}^2 + \sigma_{2i}^2}, \quad (6.2)$$

constrain the bunch observables. Owing to the higher statistics of  $pp$  interactions compared to beam-gas interactions, the constraints of Eq. (6.2) provide the most significant input to the overlap integral. Equation (6.2) is valid only for a zero crossing angle. It will be shown in Sect. 6.5.5 that the approximation is justified for this analysis.

The bunch lengths  $\sigma_{bz}$  are extracted from the longitudinal distribution of the  $pp$ -collision vertices.<sup>5</sup> Because the sizes  $\sigma_{bz}$  are approximately 1000 times larger than  $\sigma_{bx}$ , the crossing angle reduces the luminosity by a non-negligible factor equal to the first square root factor in Eq. (6.1). The case of non-collinear beams is described in more detail in Sect. 6.5.5.

The BGI method requires a vertex resolution comparable to or smaller than the transverse beam sizes. The knowledge of the vertex resolution is necessary to unfold the resolution from the measured beam profiles. The uncertainty in the resolution also plays an essential role in determining the systematic error.

The beam-gas interaction rate determines the time needed to take a *snapshot* of the beam profiles and the associated statistical uncertainty. When the time required to collect enough statistics is large compared to the time during which the beam stays stable, it becomes necessary to make additional corrections. This introduces systematic effects.

## 6.1 Data-taking conditions

The data used for the results described in the BGI analysis were taken in May 2010. In the data taken after this time the event rate was too high to select beam-gas events at the trigger level. In October a more selective trigger was in place and sufficient data could be collected. However, in this period difficulties were observed with the DCCT data for LHC filling schemes using bunch trains. One should observe that the VDM data taken in October used a dedicated fill with individually injected bunches so that these problems were not present.

In the selected fills, there were 2 to 13 bunches per beam in the machine. The number of colliding pairs at LHCb varied between 1 and 8. The trigger included a dedicated selection for events containing beam-gas interactions (see Sect. 2).

---

<sup>5</sup>In fact, only the combination  $(\sigma_{1z}^2 + \sigma_{2z}^2)$  can be obtained.

**Table 7.** LHC fills used in the BGI analysis. The third and fourth columns show the total number of (colliding) bunches  $n_{\text{tot}}$  ( $n_{\text{coll}}$ ), the fifth the typical number of particles per bunch, the sixth the period of time used for the analysis, and for the fills used in the BGI analysis the seventh and eighth the measured angles in  $x$  (in mrad) of the individual beams with respect to the LHCb reference frame (the uncertainties in the angles range from 1 to 5  $\mu\text{rad}$ ). The last two columns give the typical number of events per bunch used in the BGI vertex fits for each of the two beams.

Fill	part	ntot	$n_{\text{coll}}$	$N$	time (h)	$\alpha_{\text{beam 1}}$	$\alpha_{\text{beam 2}}$	analysis	events 1	events 2
1089		2	1	$2 \times 10^{10}$	15	0.209	-0.371	BGI 1	1270	720
1090		2	1	$2 \times 10^{10}$	4	0.215	-0.355	BGI 2	400	300
1101		4	2	$2 \times 10^{10}$	6	-0.329	0.189	BGI 3	730	400
1104	A	6	3	$2 \times 10^{10}$	5	0.211	-0.364	BGI 4	510	350
1104	B	6	3	$2 \times 10^{10}$	5	0.211	-0.364	BGI 5	520	350
1117		6	3	$2 \times 10^{10}$	6	-0.327	0.185	BGI 6	700	500
1118		6	3	$2 \times 10^{10}$	5	-0.332	0.181	BGI 7	500	400
1122		13	8	$2 \times 10^{10}$	3	-0.329	0.182	BGI 8	300	250

The HLT runs a number of algorithms designed to select beam-gas interactions with high efficiency and low background. The same vertex algorithm is used for the be, eb and bb crossings, but different  $z$ -selection cuts are applied. For bb crossings the region  $-0.35 < z < 0.25$  m is excluded to reject the overwhelming amount of  $pp$  interactions.<sup>6</sup>

## 6.2 Analysis and data selection procedure

The standard vertex reconstruction algorithms in LHCb are optimized to find  $pp$  interaction vertices close to  $z = 0$ . This preference is removed for this particular analysis such that no explicit bias is present in the track and vertex selection as a function of  $z$ . The resolution of the vertex measurement has to be known with high precision. Details of the resolution study are given in Sect. 6.3.

The BGI method relies on the unambiguous selection of beam-gas interactions, also during bb crossings where an overwhelming majority of  $pp$  collisions is present. The beam-gas fraction can be as low as  $10^{-5}$  depending on the beam conditions. The criteria to distinguish beam-gas vertices from  $pp$  interactions exploit the small longitudinal size of the beam spot (luminous region). As an additional requirement only vertices formed with exclusively forward (backward) tracks are accepted as beam 1(2)-gas interactions and vertices are required to be made with more than ten tracks. A further selection on the transverse distance from the measured beam-axis is applied to reject spurious vertices<sup>7</sup> ( $\pm 2$  mm). Due to the worsening of the resolutions for large distances from  $z = 0$  and due to the presence of  $pp$  interactions near  $z = 0$ , to determine the width of the beams the analysis regions are limited to  $-700 < z < -250$  mm for beam 1 and  $250 < z < 800$  mm for beam 2.<sup>8</sup> The selection of  $pp$  events requires  $-150 < z < 150$  mm and only accepts vertices with more than 20 tracks. The background of beam-gas interactions in the  $pp$  interaction sample is negligible owing to the high  $pp$  event rate.

<sup>6</sup>Due to the asymmetric VELO geometry, the background from  $pp$  vertices near the upstream end of the VELO is more difficult to reject, hence the asymmetric  $z$  selection.

<sup>7</sup>Interactions in material and random associations of tracks.

<sup>8</sup>The vertex resolution for beam 2 has a weaker  $z$  dependence, so the sensitivity is improved by enlarging the region.

The transverse profiles of the two beams are measured for each individual colliding bunch by projecting the vertex position on a plane perpendicular to the beam direction. The direction of the beam is determined on a fill-by-fill basis using the beam-gas interactions observed in be and eb crossings, which are free of  $pp$  interactions. The direction of the beam axis can be determined with 1 to 5  $\mu\text{rad}$  precision depending on the fill.

Out of the many LHC fills only seven are selected for the BGI analysis. It is required that all necessary data (DCCT, FBCT, luminosity counters and vertex measurements) are present during a sufficiently long period and that the bunch populations and emittances are sufficiently stable during the selected period. The list of used fills is given in Table 7. The table shows the total number of bunches and the number of bunches colliding at LHCb, the typical number of protons per bunch, the measured beam slopes with respect to the LHCb reference frame, and the duration of the period used for the analysis.

The bunch population and size cannot be assumed to be constant during the analysis period. Therefore, the DCCT and FBCT data and the vertex measurements using  $pp$  interactions are binned in periods of 900 seconds. This binning choice is not critical. The chosen value maintains sufficient statistical precision while remaining sensitive to variations of the beams. The distributions of beam-gas interactions do not have sufficient statistics and are accumulated over the full periods shown in Table 7. The analysis proceeds by determining a time-weighted average for the bunch-pair population product and the width and position of the  $pp$  beam spot. The weighting procedure solves the difficulty introduced by short periods of missing data by a logarithmic interpolation for the bunch populations and a linear interpolation for the bunch profiles. The averages defined by the latter procedure can be directly compared to the single measurement of the profiles of the single beams accumulated over the full period of multiple hours. A systematic error is assigned to account for the approximations introduced by this averaging procedure.

### 6.3 Vertex resolution

The measured vertex distribution is a convolution of the true width of each beam with the resolution function of the detector. Since the resolution is comparable to the actual beam size (approximately 35  $\mu\text{m}$  in the selected fills), it is crucial to understand this effect, and to be able to unfold it from the reconstructed values.

The vertex resolution is parametrized as a function of the multiplicity, or number of tracks used to reconstruct the vertex, and as a function of the  $z$  position of the interaction. Beam-gas vertices alone are used to measure the positions and spatial extent of each beam; however, these events are rare in comparison to beam-beam vertices. To avoid binning the beam-gas vertices in both number of tracks and  $z$  position, beam-beam events are initially used to measure the dependence of the resolution on the number of tracks. Once this dependence is known, the beam-gas vertices are used to find the  $z$  dependence of the resolution, taking into account the contribution to the resolution given by the number of tracks found in each vertex.

The resolution as a function of the number of tracks in a vertex is determined using  $pp$  interactions which occur around  $z = 0$ . The reconstructed tracks from each event are randomly split into two independent sets of equal size. The vertex reconstruction is applied to each set of tracks, and if exactly one vertex is found from each track collection it is assumed to be from the same

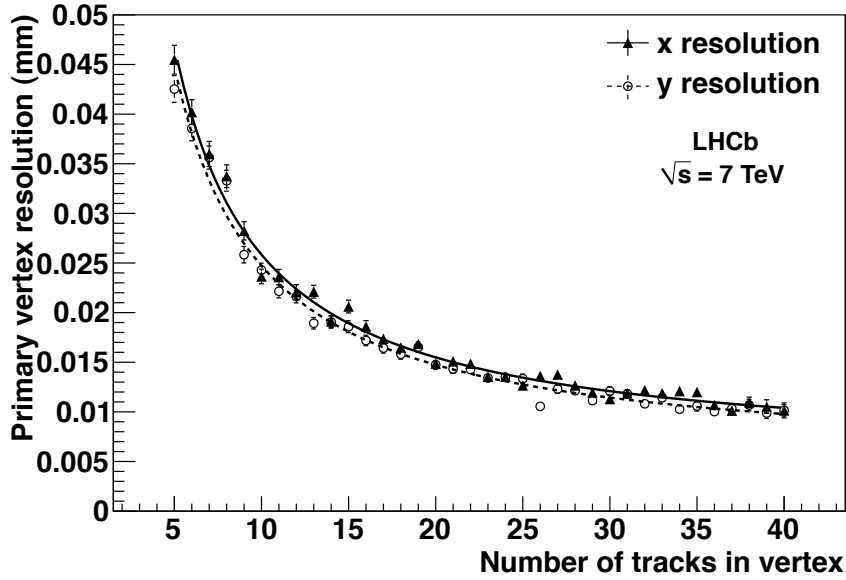


**Figure 11.** Primary vertex resolution  $\sigma_{\text{res}}$  in the transverse directions  $x$  (full circles) and  $y$  (open circles) for beam-beam interactions as a function of the number of tracks in the vertex,  $N_{\text{Tr}}$ . The curves are explained in the text.

**Table 8.** Fit parameters for the resolution of the transverse positions  $x$  and  $y$  of reconstructed beam-beam interactions as a function of the number of tracks. The errors in the fit parameters are correlated.

	$x$	$y$
Factor $A$ (mm)	$0.215 \pm 0.020$	$0.202 \pm 0.018$
Power $B$	$1.023 \pm 0.054$	$1.008 \pm 0.053$
Constant $C$ ( $10^{-3}$ mm)	$5.463 \pm 0.675$	$4.875 \pm 0.645$

original interaction. Then, if the number of tracks making each of these two vertices is the same, the residuals in  $x$  and  $y$  are taken as an estimate of the vertex resolution.

The resolution is calculated as the width of the Gaussian function fitted to the residual distributions divided by  $\sqrt{2}$ , as there are two resolution contributions in each residual measurement. The resolutions are shown as a function of the number of tracks in Fig. 11. Since the VELO is not fully symmetric in the  $x$  and  $y$  coordinates, the analysis is performed in both coordinates separately. Indeed, one observes a small, but significant difference in the resolution. The points of Fig. 11 are fitted with a function which parametrizes the resolution in terms of a factor  $A$ , a power  $B$  and a constant  $C$ , as a function of the track multiplicity  $N_{\text{Tr}}$

$$\sigma_{\text{res}} = \frac{A}{N_{\text{Tr}}^B} + C. \quad (6.3)$$

The values of the fit parameters are given in Table 8.

Beam-gas vertices, selected in be and eb bunch crossings, are reconstructed in the same manner as the  $pp$  vertices. Every beam-gas event which yields two vertices after splitting the track

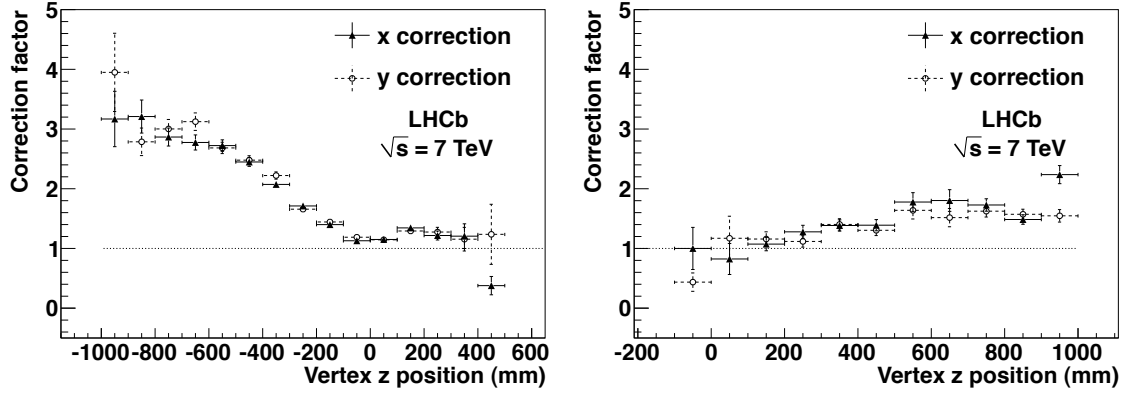


**Figure 12.** The  $z$  dependence of the resolution correction factor  $F_z$  in  $x$  (full circles) and  $y$  (open circles) for beam 1-gas (left) and beam 2-gas (right) interactions.

sample into two is used in the analysis, without requiring that the two vertices are reconstructed with an equal number of tracks. Accounting for the resolution coming from the track multiplicity means that a correction factor  $F_z$  is calculated as a function of  $z$  position. This is the factor by which the beam-beam resolution at  $z = 0$  must be multiplied to find the true resolution for an event with a particular number of tracks, at a certain position in  $z$ . The contribution to the resolution from the track multiplicity is taken into account for coordinate  $v$  ( $v = x, y$ ) according to

$$F_z = \frac{v_1 - v_2}{\sqrt{\sigma_{N_{Tr_1}}^2 + \sigma_{N_{Tr_2}}^2}}, \quad (6.4)$$

where the index 1,2 signifies the two vertices with measured position  $v_1$  and  $v_2$ , and  $N_{Tr_1}, N_{Tr_2}$  the number of tracks in each. The quantities  $\sigma_{N_{Tr_{1,2}}}$  are the resolutions  $\sigma_{res}$  expected for vertices at  $z = 0$  made of  $N_{Tr}$  tracks as defined in Eq. 6.3.

The correction factors  $F_z$  are plotted in Fig. 12. In order to better understand the resolution as a function of  $z$ , it is instructive to consider the geometry of the VELO, shown in Fig. 1. Figure 12 shows that around the interaction point of  $z = 0$  the correction factor is close to one, which signifies that the resolution is nearly independent of the type of event, whether beam-beam or beam-gas. This is expected, since the VELO is optimized to reconstruct vertices near  $z = 0$ . The correction factor increases as the vertices move away from the interaction region.

#### 6.4 Measurement of the beam profiles using the BGI method

In Fig. 13 the positions of the vertices of beam-gas interactions of the single beams in be and eb crossings are shown in the  $x$ - $z$  and  $y$ - $z$  planes. The straight line fits provide the beam angles in the corresponding planes. Whereas we can use the non-colliding bunches to determine the beam directions, the colliding bunches are the only relevant ones for luminosity measurements.

As an example the  $x$  and  $y$  profiles of one colliding bunch pair are shown in Fig. 14. The physical bunch size is obtained after deconvolving the vertex resolution. The resolution function and physical beam profile are drawn separately to show the importance of the knowledge of the resolution. In Fig. 15 the corresponding fits to the luminous region of the same bunch pair are



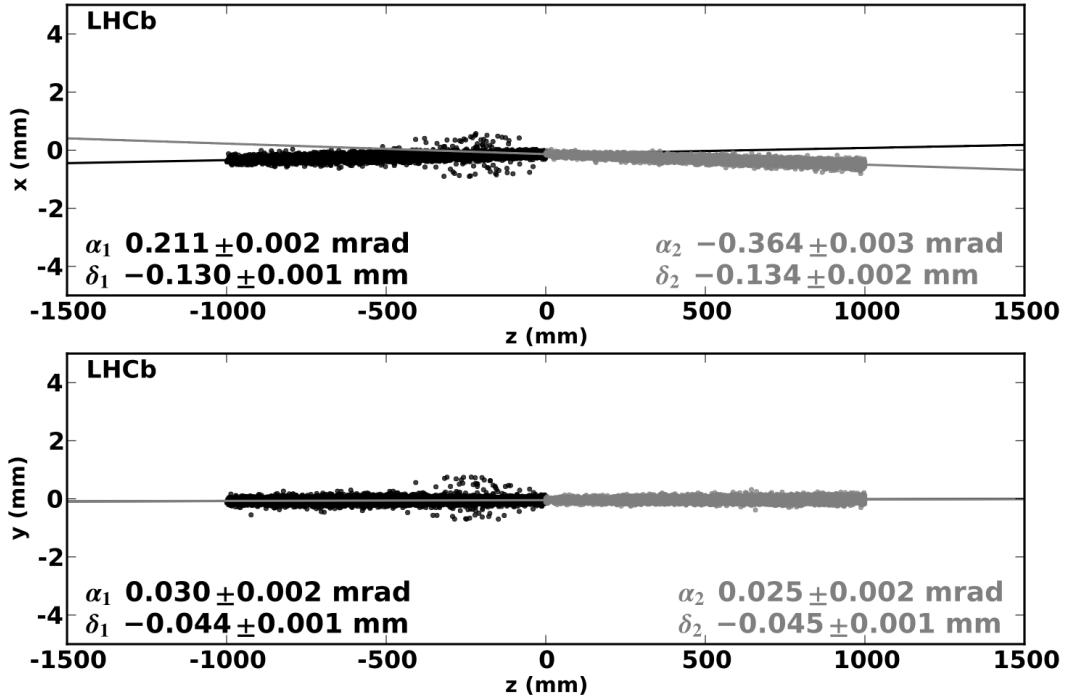


**Figure 13.** Positions of reconstructed beam-gas interaction vertices for be (black points) and eb (grey points) crossings during Fill 1104. The measured beam angles  $\alpha_{1,2}$  and offsets  $\delta_{1,2}$  at  $z = 0$  in the horizontal (top) and vertical (bottom) planes are shown in the figure.

shown, both for the full fill duration and for a short period of 900 s. The fits to the distributions in  $x$  and  $y$  of the full fill have a  $\chi^2/\text{ndf} \approx 10$ , probably due to the emittance growth of the beam. The corresponding fits to data taken during the shorter period of 900 s give satisfactory values,  $\chi^2/\text{ndf} \approx 1$ . The fact that the resolution at  $z = 0$  is small compared to the size of the luminous region makes it possible to reach small systematic uncertainties in the luminosity determination as shown in Sect. 6.6.

For non-colliding bunches it is possible to measure the width of the beam in the region of the interaction point at  $z = 0$  since there is no background from  $pp$  collisions. One can compare the measurement at the IP with the measurement in the region outside the IP which needs to be used for the colliding bunches. After correcting for the resolution no difference is observed, as expected from the values of  $\beta^*$  of the beam optics used during the data taking. One can also compare the width measurements of the colliding bunches far from the IP using the beam-gas events from beam 1 and beam 2 to predict the width of the luminous region using Eq. 6.2. Figure 16 shows that there is overall consistency. In addition to the data used in the BGI analysis described here, also higher statistics data from later fills are used for this comparison. The cross check reaches a precision of 1–1.6% for the consistency of the width measurements at large  $z$  compared to the measurement at  $z = 0$ , providing good evidence for the correctness of the parametrization of the  $z$  dependence of the vertex resolution.

The relations of Eq. 6.2 are used to constrain the width and position measurements of the

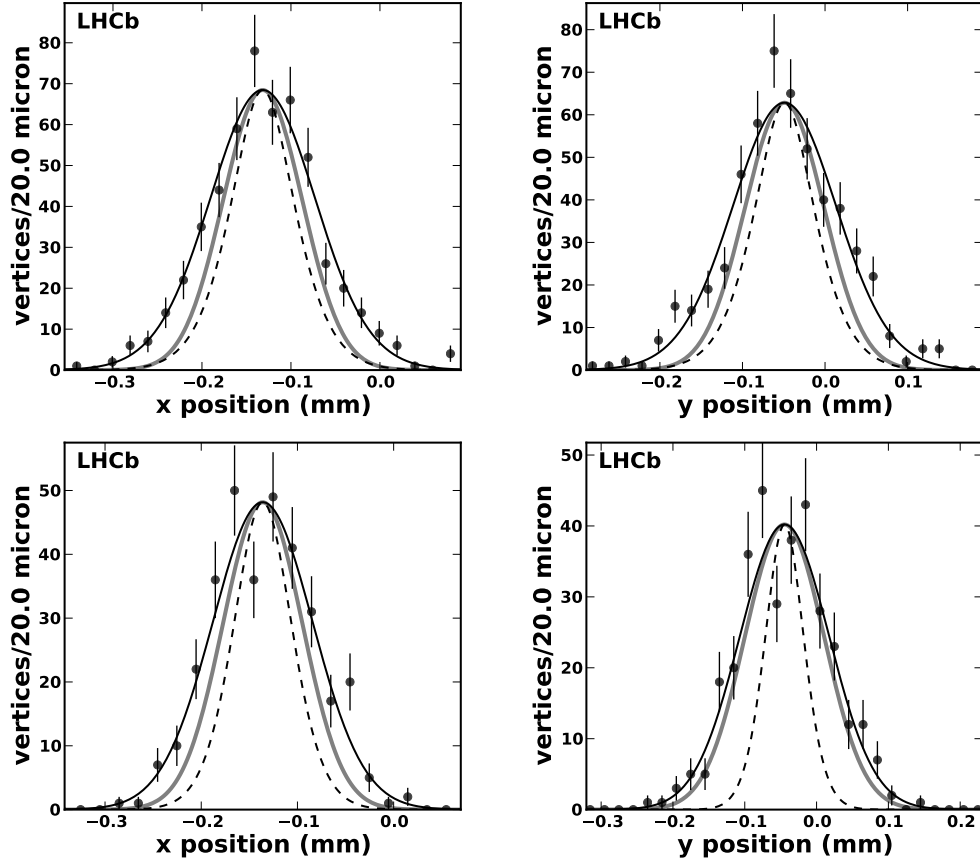


**Figure 14.** Distributions of the vertex positions of beam-gas events for beam 1 (top) and beam 2 (bottom) for one single bunch pair (ID 2186) in Fill 1104. The left (right) panel shows the distribution in  $x$  ( $y$ ). The Gaussian fit to the measured vertex positions is shown as a solid black curve together with the resolution function (dashed) and the unfolded beam profile (shaded). Note the variable scale of the horizontal axis.

single beams and of the luminous region in both coordinates separately. Given the high statistics of vertices of the luminous region the  $pp$  events have the largest weight in the luminosity calculation. Effectively, the beam-gas measurements determine the relative offsets of the two beams and their width ratio  $\rho$

$$\rho_i = \sigma_{2i}/\sigma_{1i} \quad (i = x, y). \quad (6.5)$$

According to Eq. 6.1, neglecting crossing angle effects and beam offsets, the luminosity is proportional to  $A_{\text{eff}}^{-1}$ ,

$$A_{\text{eff}}^{-1} = \frac{1}{\sqrt{(\sigma_{1x}^2 + \sigma_{2x}^2)(\sigma_{1y}^2 + \sigma_{2y}^2)}}. \quad (6.6)$$

This quantity can be rewritten using the definition of  $\rho_i$  and Eq. 6.2

$$A_{\text{eff}}^{-1} = \prod_{i=x,y} \frac{\rho_i}{(1 + \rho_i^2)\sigma_{\otimes i}}, \quad (6.7)$$

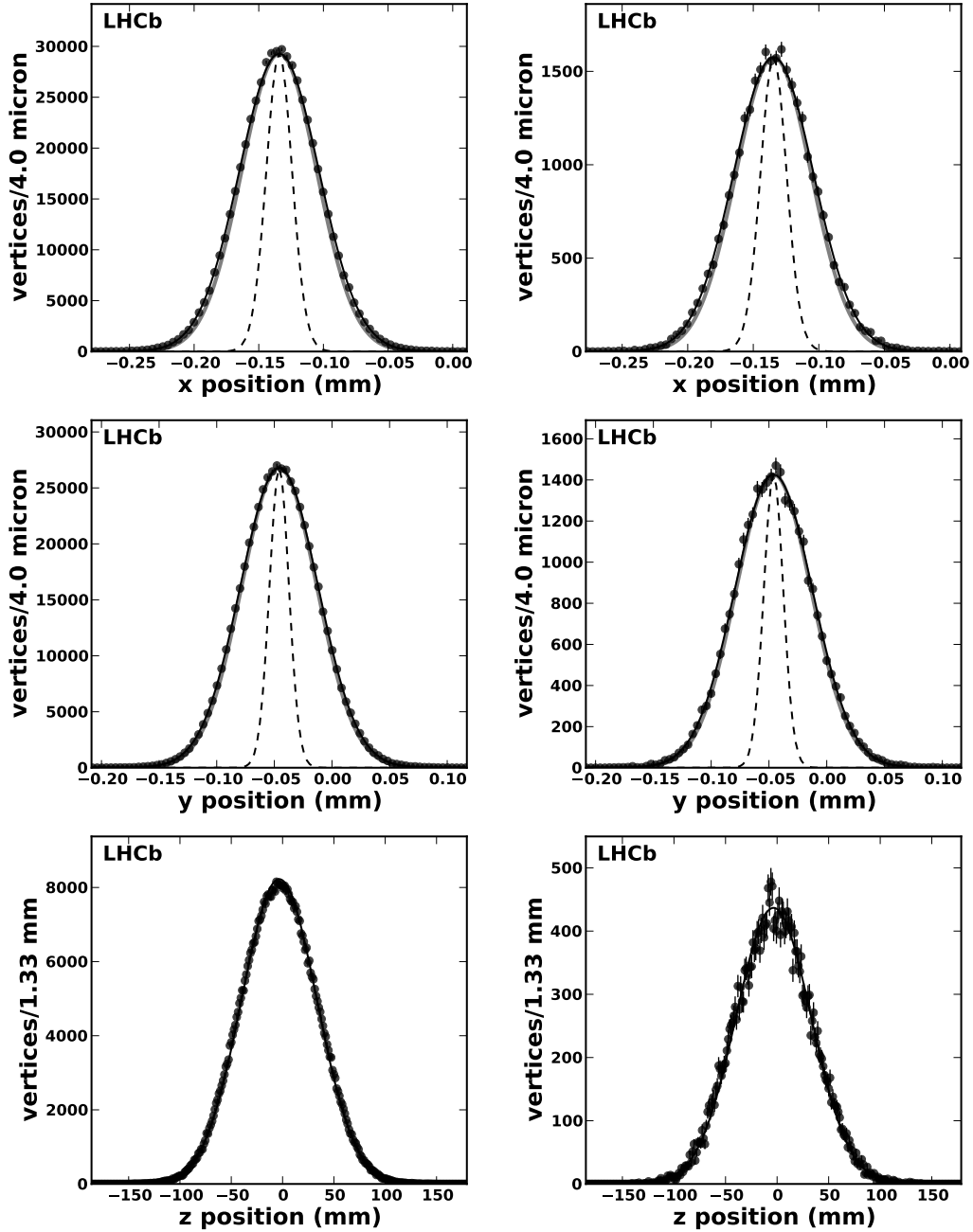


**Figure 15.** Distributions of vertex positions of  $pp$  interactions for the full fill duration (left) and for a 900 s period in the middle of the fill (right) for one colliding bunch pair (ID 2186) in Fill 1104. The top, middle and bottom panels show the distributions in  $x$ ,  $y$  and  $z$ , respectively. The Gaussian fit to the measured vertex positions is shown as a solid black curve together with the resolution function (dashed) and the unfolded luminous region (shaded). Owing to the good resolution the shaded curves are close to the solid curves and are therefore not clearly visible in the figures. The fit to the  $z$  coordinate neglects the vertex resolution. Note the variable scale of the horizontal axis.

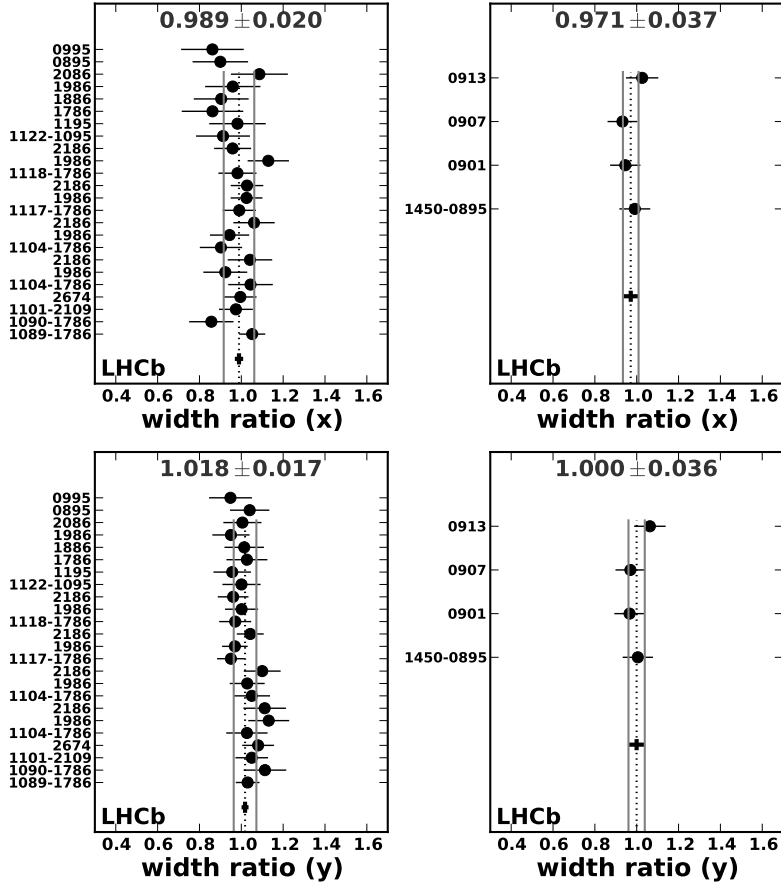


**Figure 16.** Comparison of the prediction for the luminous region width from measurements based on beam-gas events of individual bunches which are part of a colliding bunch pair with the direct measurement of the luminous region width for these colliding bunches. The panels on the left show the results for bunches in the fills with  $\beta^* = 2$  m optics used in this analysis, the right panels show four colliding bunches in a fill taken with  $\beta^* = 3.5$  m optics. The fill and bunch numbers are shown on the vertical axis. The vertical dotted line indicates the average and the solid lines the standard deviation of the data points. The lowest point indicates the weighted average of the individual measurements; its error bar represents the corresponding uncertainty in the average. The same information is given above the data points. The fills with the  $\beta^* = 3.5$  m optics are not used for the analysis due to the fact that larger uncertainties in the DCCT calibration were observed.

which shows, especially for nearly equal beam sizes, the weight of the measurement of the width of the luminous region  $\sigma_{\otimes i}$  in the luminosity determination. The expression has its maximum for  $\rho_i = 1$  which minimizes the importance of the measurement errors of  $\rho_i$ .

The luminosity changes if there is an offset between the two colliding bunches in one of the transverse coordinates. An extra factor appeared already in Eq. 6.1 to take this into account

$$C_{\text{offset}} = \prod_{i=x,y} \exp\left(-\frac{1}{2} \frac{(\xi_{1i} - \xi_{2i})^2}{\sigma_{1i}^2 + \sigma_{2i}^2}\right), \quad (6.8)$$

which is unity for head-on beams.

By examining both relations of Eq. 6.2 a system of two constraint equations and six measurable quantities emerges which can be used to improve the precision for each transverse coordinate separately. This fact is exploited in a combined fit where the individual beam widths  $\sigma_{1i}$ ,  $\sigma_{2i}$ , and the luminous region width  $\sigma_{\otimes i}$  together with the corresponding position values  $\xi_{bi}$  and  $\xi_{\otimes i}$  are used as input measurements. Several choices are possible for the set of four fit-parameters, trivially the set  $\sigma_{1i}$ ,  $\sigma_{2i}$ ,  $\xi_{1i}$ ,  $\xi_{2i}$  can be used. The set  $\Sigma_i$  (Eq. 5.5),  $\rho_i$  (Eq. 6.5),  $\Delta\xi_i = \xi_{1i} - \xi_{2i}$  and  $\xi_{\otimes i}$  is used which makes it easier to evaluate the corresponding luminosity error propagation. The results for the central values are identical, independently of the set used.

## 6.5 Corrections and systematic errors

In the following, corrections and systematic error sources affecting the BGI analysis will be described. The uncertainties related to the bunch population normalization have already been discussed in Sect. 4.

### 6.5.1 Vertex resolution

As mentioned above, the uncertainty of the resolution potentially induces a significant systematic error in the luminosity measurement. To quantify its effect the fits to the beam profiles have been made with different choices for the parameters of the resolution functions within the limits of their uncertainty. One way to estimate the uncertainty is by comparing the resolution of simulated  $pp$  collision events determined using the method described in Sect. 6.3, *i.e.* by dividing the tracks into two groups, with the true resolution which is only accessible in the simulation owing to the prior knowledge of the vertex position. The uncertainty in the number of tracks ( $N_{Tr}$ ) dependence at  $z = 0$  is estimated in this way to be no larger than 5%.

The uncertainty in the  $z$  dependence is estimated by analysing events in eb and be crossings. For these crossings all events, including the ones near  $z = 0$ , can be assumed to originate from beam-gas interactions. A cross check of the resolution is obtained by comparing the measurement of the transverse beam profiles at the  $z$  range used in bb events with the ones obtained near  $z = 0$ . Together with the comparison of the width of the luminous region and its prediction from the beam-gas events we estimate a 10% uncertainty in the  $z$  dependence of the resolution. It should be noted that the focusing effect of the beams towards the interaction point is negligible compared to the precision needed to determine the resolution.

The effect of the uncertainties in the  $N_{Tr}$  dependence and  $z$  dependence on the final results are estimated by repeating the analysis varying the resolution within its uncertainty. The conservative approach is taken to vary the different dependencies coherently in both  $x$  and  $y$  and for the dependence on  $N_{Tr}$  and  $z$  simultaneously. The resulting uncertainties in the cross-section depend on the widths of the distributions and are therefore different for each analysed bunch pair.

### 6.5.2 Time dependence and stability

The beam and data-taking stability are taken into account when selecting suitable fills to perform the beam-gas imaging analysis. This is an essential requirement given the long integration times needed to collect sufficient statistics for the beam-gas interactions. A clear decay of the bunch-populations and emittance growth is observed over these long time periods. It is checked that these

variations are smooth and that the time-average is a good approximation to be used to compare with the average beam profiles measured with vertices of beam-gas interactions. No significant movement of the luminous region is observed during the fills selected for the BGI analysis. The systematics introduced by these variations are minimized by the interpolation procedure described in Sect. 6.2 and are estimated to amount to less than 1%.

### 6.5.3 Bias due to unequal beam sizes and beam offsets

When the colliding bunches in a pair have similar widths ( $\rho_i = 1$ ), the  $\rho$ -dependence in Eq. 6.7,  $\rho_i/(1 + \rho_i^2)$ , is close to its maximum. Thus, when the precision of measuring  $\rho$  is similar to its difference from unity, the experimental estimate of the  $\rho$ -factor is biased towards smaller values. In the present case the deviation from unity is compatible with the statistical error of the measurement for each colliding bunch pair. These values are typically 15% in the  $x$  coordinate and 10% in the  $y$  coordinate. The size of the “ $\rho$  bias” effect is of the order of 1% in  $x$  and 0.5% in  $y$ .

A similar situation occurs for the offset factor  $C_{\text{offset}}$  for bunches colliding with non-zero relative transverse offset. The offsets are also in this case compatible with zero within their statistical errors and the correction can only take values smaller than one. The average expected “offset bias” is typically 0.5% per transverse coordinate.

Since these four sources of bias (unequal beam sizes and offsets in both transverse coordinates) act in the same direction, their overall effect is no longer negligible and is corrected for on a bunch-by-bunch basis. We assume a systematic error equal to half of the correction, *i.e.* typically 1.5%. The correction and associated uncertainty depends on the measured central value and its statistical precision and therefore varies per fill.

### 6.5.4 Gas pressure gradient

The basic assumption of the BGI method is the fact that the residual gas pressure is uniform in the plane transverse to the beam direction and hence the interactions of the beams with the gas produce an image of the beam profile. An experimental verification of this assumption is performed by displacing the beams and recording the rate of beam-gas interactions at these different beam positions. In Fill 1422 the beam was displaced in the  $x$  coordinate by a maximum of 0.3 mm. Assuming a linear behaviour, the upper limit on the gradient of the interaction rate is 0.62 Hz/mm at 95% CL compared to a rate of  $2.14 \pm 0.05$  Hz observed with the beam at its nominal position. When the profiles of beam 1-gas and beam 2-gas interactions are used directly to determine the overlap integral  $A_{\text{eff}}$ , the relative error  $\delta_A$  on the overlap integral is given by

$$\delta_A = \frac{A_{\text{eff}}(a = 0)}{A_{\text{eff}}(a \neq 0)} - 1 = \frac{a^2 \sigma_x^2}{2b^2}, \quad (6.9)$$

where  $a$  is the gradient,  $b$  the rate when the beam is at its nominal position, and  $\sigma_x$  is the true beam width, using the approximation of equal beam sizes. This result has been derived by comparing the overlap integral for beam images distorted by a linear pressure gradient with the one obtained with ideal beam images. With the measured limit on the gradient, the maximum relative effect on the overlap is then estimated to be less than  $4.2 \times 10^{-4}$ . However, the BGI method uses the width of the luminous region measured using  $pp$  interactions as a constraint. This measurement does not depend on the gas pressure gradient. The gas pressure gradient enters through the measurements of

the individual widths which are mainly used to determine the ratio between the two beam widths. These are equally affected, thus, the overall effect of an eventual gas pressure gradient is much smaller than the estimate from Eq. 6.9 and can safely be neglected in the analysis.

### 6.5.5 Crossing angle effects

The expression for the luminosity (Eq. 6.1) contains a correction factor for the crossing angle  $C_\alpha$  of the form [24]

$$C_\alpha = [1 + \tan^2 \alpha (\sigma_{1z}^2 + \sigma_{2z}^2) / (\sigma_{1x}^2 + \sigma_{2x}^2)]^{-\frac{1}{2}}. \quad (6.10)$$

For a vanishing crossing angle and equal bunch lengths, the bunch length  $\sigma_z$  is obtained from the beam spot measurement assuming that the two beams have equal size, by  $\sigma_z = \sqrt{2} \sigma_{\otimes z}$ . In the presence of a crossing angle the measured length of the luminous region depends on the lengths of the bunches, on the crossing angle and on the transverse widths of the two beams in the plane of the crossing angle. The bunch lengths need not necessarily be equal. Evaluating the overlap integral of the two colliding bunches over the duration of the bunch crossing, one finds for the width of the luminous region in the  $z$  coordinate

$$\sigma_{\otimes z} = \left[ \frac{\tan^2 \alpha}{\sigma_{\otimes x}^2} + \frac{4 \cos^2 \alpha}{\sigma_{1z}^2 + \sigma_{2z}^2} \right]^{-\frac{1}{2}}. \quad (6.11)$$

Solving for  $\sigma_{1z}^2 + \sigma_{2z}^2$ , the right-hand side of Eq. 6.10 can be written in terms of the measured quantities  $\alpha$ ,  $\sigma_{\otimes z}$ ,  $\sigma_{\otimes x}$ ,  $\sigma_{1x}$ , and  $\sigma_{2x}$

$$C_\alpha = \left[ 1 + \frac{4 \sin^2 \alpha \sigma_{\otimes z}^2}{(1 - (\tan \alpha \sigma_{\otimes z} / \sigma_{\otimes x})^2) (\sigma_{1x}^2 + \sigma_{2x}^2)} \right]^{-\frac{1}{2}}. \quad (6.12)$$

The dependence of the estimate of  $\sigma_{\otimes z}$  on  $\sigma_z$  and of the overall correction on  $\sigma_x$  is shown in Fig. 17 for typical values of the parameters. The difference with respect to a naive calculation assuming equal beam sizes and using the simple  $\sqrt{2}$  factor to obtain the bunch lengths from the luminous region length is in all relevant cases smaller than 1%. For the beam conditions in May 2010 the value of the crossing angle correction factor  $C_\alpha$  is about 0.95. To take into account the accuracy of the calculation a 1% systematic error is conservatively assigned to this factor.

There are other small effects introduced by the beam angles. The average angle of the beams is different from 0 in the LHCb coordinate system. This small difference introduces a broadening of the measured transverse widths of the luminous region, since in this case the projection is taken along the nominal LHCb axis. Another effect is more subtle. The expression (Eq. 6.2) for the width of the luminous region assumes a vanishing crossing angle. It is still valid for any crossing angle if one considers the width for a fixed value of  $z$ . When applying Eq. 6.2 as a function of  $z$  one can show that the centre of the luminous region is offset if in the presence of a non-vanishing crossing angle the widths of the two beams are not equal. Thus, when these two conditions are met the luminous region is rotated. The rotation angle  $\phi_i$  ( $i = x, y$ ) is given by

$$\tan \phi_i = \tan \alpha_i \frac{1 - \rho_i^2}{1 + \rho_i^2}, \quad (6.13)$$

where  $\rho$  is defined in Eq. 6.5. With the parameters observed in this analysis the effect of the rotation is smaller than  $10^{-3}$ .

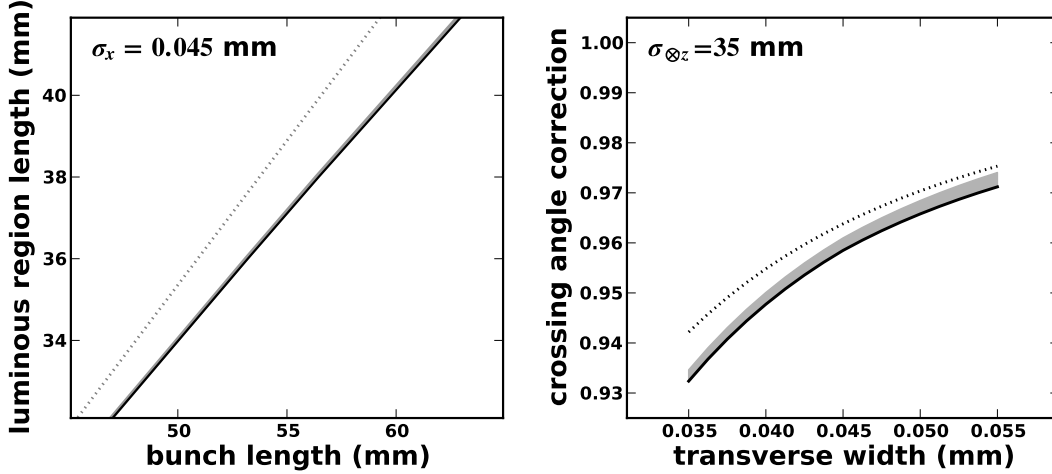


**Figure 17.** Left: the dependence of the length of the luminous region  $\sigma_{\otimes z}$  on the single bunch length  $\sigma_z$  under the assumption that both beams have equal length bunches. The dotted line shows the  $\sqrt{2}$  behaviour expected in the absence of a crossing angle. The solid black line shows the dependence for equal transverse beam sizes  $\sigma_x = 0.045$  mm, the shaded region shows the change for  $\rho = 1.2$  keeping the average size constant. Right: the dependence of the luminosity reduction factor  $C_\alpha$  on the transverse width of the beam  $\sigma_x$  for a value of  $\sigma_{\otimes z} = 35$  mm. The solid line shows the full calculation for  $\rho = 1$  (equal beam widths) with the shaded area the change of the value up to  $\rho = 1.2$ , keeping the transverse luminous region size constant. The dotted line shows the result of the naive calculation assuming a simple  $\sqrt{2}$  relation for the length of the individual beams. All graphs are calculated for a half crossing-angle  $\alpha = 0.2515$  mrad.

## 6.6 Results of the beam-gas imaging method

With the use of the beam-gas imaging method seven independent measurements of an effective reference cross-section were performed. The main uncertainties contributing to the overall precision of the cross-section measurement come from the overlap integral and from the measurement of the product of the bunch populations. The systematic error in the overlap integral is composed of the effect of the resolution uncertainties, the treatment of the time dependence, the treatment of the bias due to the non-linear dependencies in  $\rho$  and  $\Delta(\xi)$  and the crossing angle corrections. It also takes into account small deviations of the beam shape from a single Gaussian observed in the VDM scans. The normalization error has components from the DCCT scale, and its baseline fluctuations, FBCT systematics, and systematics in the relative normalization procedure (Sect. 3). For multi-bunch fills the results obtained for each colliding pair are first averaged taking the correlations into account. The results of the averaging procedure applied on a per-fill basis are shown in Table 9. For fills with multiple bunches the numbers are a result of an average over individual bunches. Errors are divided into two types: correlated and uncorrelated errors. On a fill-by-fill basis the statistical errors, ghost charge and DCCT baseline corrections are treated as uncorrelated errors. The latter two sources are of course correlated when bunches within one fill are combined. The FBCT systematic uncertainty, which is dominated by the uncertainty in its offset is treated taking into account the fact that the sum is constrained. Owing to the constraint on the total beam current provided by the DCCT, averaging results for different colliding bunch pairs within one fill



**Table 9.** Measurements of the cross-section  $\sigma_{\text{vis}}$  with the BGI method per fill and overall average (third column). All errors are quoted as percent of the cross-section values. *DCCT scale*, *DCCT baseline noise*, *FBCT systematics* and *Ghost charge* are combined into the overall *Beam normalization* error. The *Width syst* row is the combination of *Resolution syst* (the systematic error in the vertex resolution for *pp* and beam-gas events), *Time dep. syst* (treatment of time-dependence) and *Bias syst* (unequal beam sizes and beam offset biases), and is combined with *Crossing angle* (uncertainties in the crossing angle correction) into *Overlap syst*. The *Total error* is the combination of *Relative normalization stability*, *Beam normalization*, *Statistical error*, and *Overlap syst*. *Total systematics* is the combination of the latter three only and can be broken down into *Uncorrelated syst* and *Correlated syst*, where “uncorrelated” applies to the averaging of different fills. Finally, *Excluding norm* is the uncertainty excluding the overall *DCCT scale* uncertainty. The grouping of the systematic errors into (partial) sums is expressed as an indentation in the first column of the table. The error components are labelled in the second column by *u*, *c* or *f* depending on whether they are uncorrelated, fully correlated or correlated within one fill, respectively.

		<b>average</b>	<b>1089</b>	<b>1090</b>	<b>1101</b>	<b>1104</b>	<b>1117</b>	<b>1118</b>	<b>1122</b>
Cross-section $\sigma_{\text{vis}}$ (mb)		<b><u>59.94</u></b>	61.49	59.97	57.67	56.33	61.63	61.84	61.04
Relative normalization stability	<i>c</i>	0.50	0.50	0.50	0.50	0.50	0.50	0.50	0.50
DCCT scale	<i>c</i>	2.70	2.70	2.70	2.70	2.70	2.70	2.70	2.70
DCCT baseline noise	<i>f</i>	0.36	0.97	1.01	0.43	0.29	0.29	0.29	0.14
FBCT systematics	<i>f</i>	0.91	3.00	3.00	2.61	2.10	2.41	2.41	1.98
Ghost charge	<i>f</i>	0.19	0.70	0.65	1.00	0.60	0.38	0.55	0.35
Beam normalization		2.88	4.21	4.21	3.91	3.48	3.65	3.67	3.37
Statistical error	<i>u</i>	0.96	4.06	4.73	3.09	2.56	1.89	2.66	1.82
Resolution syst	<i>c</i>	2.56	2.79	2.74	2.54	2.86	2.37	2.47	2.44
Time dep. syst	<i>c</i>	1.00	1.00	1.00	1.00	1.00	1.00	1.00	1.00
Bias syst	<i>c</i>	1.61	1.14	1.81	1.35	1.89	1.19	1.35	2.05
Gas homogeneity		negl.	negl.	negl.	negl.	negl.	negl.	negl.	negl.
Width syst		3.20	3.18	3.43	3.05	3.56	2.83	2.99	3.34
Crossing angle	<i>c</i>	1.00	1.00	1.00	1.00	1.00	1.00	1.00	1.00
Overlap syst		3.35	3.33	3.58	3.21	3.70	3.00	3.15	3.49
Uncorrelated syst	<i>f</i>	0.93	3.08	3.07	2.80	2.18	2.44	2.47	2.01
Correlated syst	<i>c</i>	4.35	4.43	4.62	4.25	4.62	4.08	4.19	4.44
Total systematics		4.45	5.39	5.55	5.08	5.11	4.75	4.87	4.88
Total error		4.55	6.75	7.29	5.95	5.71	5.11	5.55	5.20
Excluding norm		3.63	6.17	6.75	5.28	5.01	4.31	4.82	4.42

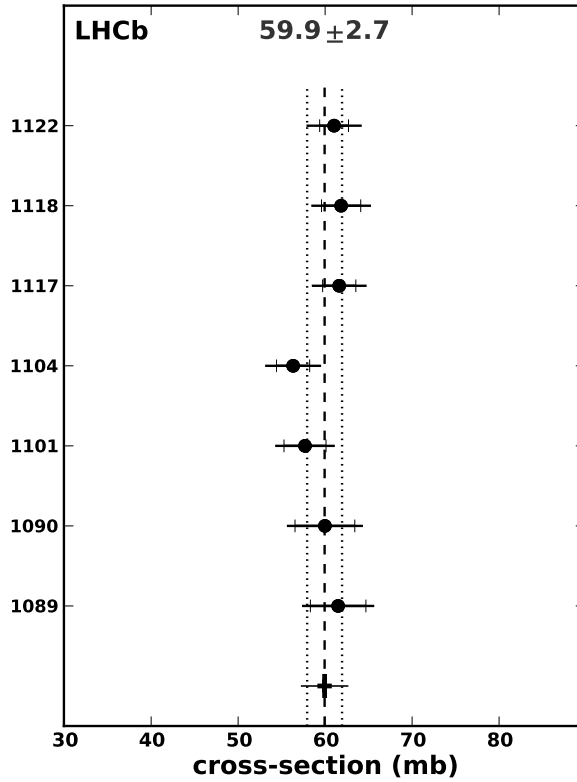


**Figure 18.** Results of the beam-gas imaging method for the visible cross-section of the  $pp$  interactions producing at least two VELO tracks,  $\sigma_{\text{vis}}$ . The results for each fill (indicated on the vertical axis) are obtained by averaging over all colliding bunch pairs. The small vertical lines on the error bars indicate the size of the uncorrelated errors, while the length of the error bars show the total error. The dashed vertical line indicates the average of the data points and the dotted vertical lines show the one standard-deviation interval. The weighted average is represented by the lowest data point, where the error bar corresponds to its total error.

reduces the error introduced by the FBCT offset uncertainty. A usual error propagation is applied taking the inverse square of the uncorrelated errors as the weights. The difference with respect to the procedure applied for the VDM method is due to the fact that a fit using the FBCT offsets as free parameters cannot be applied here. Not all fills have the required number of crossing bunch pairs, and the uncorrelated bunch-to-bunch errors are too large to obtain a meaningful result for the FBCT offset.

Each colliding bunch pair provides a self-consistent effective cross-section determination. The analysis proceeds by first averaging over all individual colliding bunch pairs within a fill and then by averaging over fills taking all correlations into account. Thus, an effective cross-section result can also be quoted per fill. These are shown in Fig. 18. The spread in the results is in good agreement with the expectations from the uncorrelated errors.

The final beam-gas result for the effective cross-section is:  $\sigma_{\text{vis}} = 59.9 \pm 2.7$  mb. The uncertainties in the DCCT scale error and the systematics of the relative normalization procedure are in common with the VDM method. The uncertainty in  $\sigma_{\text{vis}}$  from the BGI method without these common errors is 2.2 mb.

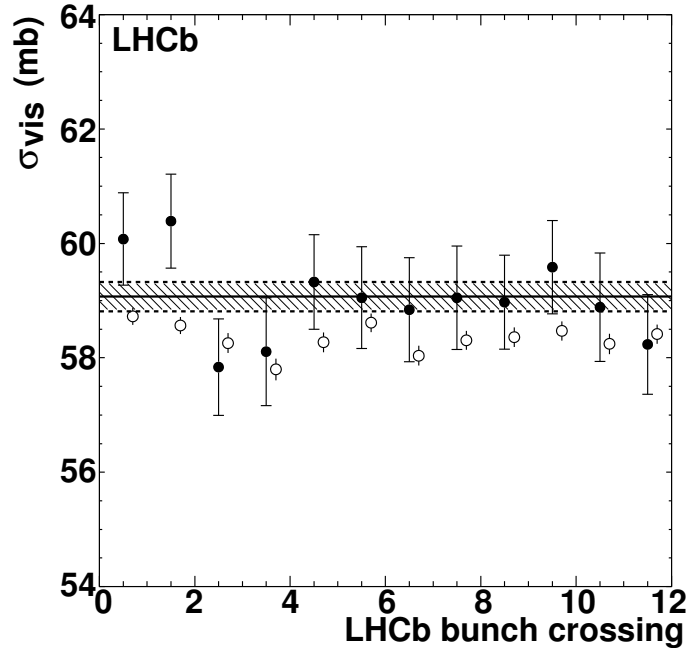


**Figure 19.** Visible cross-section measurement using the beam-beam imaging method for twelve different bunch pairs (filled circles) compared to the cross-section measurements using the VDM method (open circles). The horizontal line represents the average of the twelve beam-beam imaging points. The error bars are statistical only and neglect the correlations between the measurements of the profiles of two beams. The band corresponds to a one sigma variation of the vertex resolution parameters.

## 7. Cross checks with the beam-beam imaging method

During the VDM scan the transverse beam images can be reconstructed with a method described in Ref. [15]. When one beam (*e.g.* beam 1) scans across the other (beam 2), the differences of the measured coordinates of  $pp$  vertices with respect to the nominal position of beam 2 are accumulated. These differences are projected onto a plane transverse to beam 2 and summed over all scan points. The resulting distribution represents the density profile of beam 2 when the number of scan steps is large enough and the step size is small enough. By inverting the procedure, beam 1 can be imaged using the relative movement of beam 2. Since the distributions are obtained using measured vertex positions, they are convolved with the corresponding vertex resolution. After deconvolving the vertex distributions with the transverse vertex resolution a measurement of the transverse beam image is obtained. This approach is complementary to the BGI and VDM methods.

The beam-beam imaging method is applied to the first October VDM scan since the number of scanning steps of that scan is twice as large as that of the second scan. The events are selected by the minimum bias trigger. Contrary to the 22.5 kHz random trigger events with only luminosity data, they contain complete detector information needed for the tracking. The minimum-bias trigger rate was limited to about 130 Hz on average. The bias due to the rate limitation is corrected by normalizing the vertex distributions at every scan point to the measured average number of interactions per crossing.

The transverse planes with respect to the beams are defined using the known half crossing-

angle of  $170 \mu\text{rad}$  and the measured inclination of the luminous ellipsoid with respect to the  $z$  axis as discussed in Sect. 5.3.3. The measured common length scale correction and the difference in the length scales of the two beams described by the asymmetry parameters  $\epsilon_{x,y}$  in Eq. 5.3, are also taken into account.

The luminosity overlap integral is calculated numerically from the reconstructed normalized beam profiles. The effect of the VELO smearing is measured and subtracted by comparing with the case when the smearing is doubled. The extra smearing is performed on an event-by-event basis using the description of the resolution given in Eq. 6.3 with the parameters  $A$ ,  $B$  and  $C$  taken from Table 8. To improve the vertex resolution, only vertices made with more than 25 tracks are considered. This reduces the average cross-section correction due to the VELO resolution to 3.7%.

Similar to the BGI method, the beam-beam imaging method measures the beam profiles perpendicular to the beam directions. For the luminosity determination in the presence of a crossing angle their overlap should be corrected by the factor  $C_\alpha$  (see Eq. 6.10) due to a contribution from the length of the bunches. The average correction for the conditions during the VDM fill in October is 2.6%. A bunch-by-bunch comparison of the cross-section measurement with the beam-beam imaging method and the VDM method is shown in Fig. 19. The cross-section is measured at the nominal beam positions. The FBCT bunch populations with zero offsets normalized to the DCCT values and corrected for the ghost charge are used for the cross-section determination. The band indicates the variation obtained by changing the vertex resolution by one standard deviation in either direction. The obtained cross-section of 59.1 mb is in good agreement with the value of 58.4 mb reported in Table 4. The comparison is very sensitive since the overall bunch population normalization and the length scale uncertainty are in common. Uncorrelated errors amount to about 1%. The main uncorrelated errors in the beam-beam imaging method are the VELO systematics and the statistical error which are each at the level of 0.4%. The main uncorrelated errors in the VDM method are the stability of the working point (0.4%) and the statistics (0.1%). The difference between the two methods is smaller than but similar to the difference between the two October scan results observed with the VDM method.

The width of the VDM rate profile and the widths of the individual beams are related following Eq. 5.5. Thus the widths  $\Sigma_{x,y}$  are directly *measured* with the VDM rate profile and *predicted* using the measured widths of the beams. The widths can be compared directly using the RMS of the distributions, the widths (RMS) of single Gaussian fits or the RMS of double Gaussian fits. The variation among these different values are of the order of 1% and limit the sensitivity. However, it should be noted that these are just numerical differences; Eq. 5.5 holds for arbitrary beam shapes. The ratio of the measured and predicted width is 0.994 and 0.996 in the  $x$  and  $y$  coordinate, respectively. The statistical uncertainties are 0.3% and the uncertainties due to the knowledge of the vertex resolution are 0.2%. Considering the sensitivity of the comparison, we note good agreement.

## 8. Results and conclusions

The beam-gas imaging method is applied to data collected by LHCb in May 2010 using the residual gas pressure and provides an absolute luminosity normalization with a relative uncertainty of 4.6%, dominated by the knowledge of the bunch populations. The measured effective cross-section is in

**Table 10.** Averaging of the VDM and BGI results and additional uncertainties when applied to data-sets used in physics analyses.

	<b>Average</b>	<b>VDM</b>	<b>BGI</b>
Cross-section (mb)	58.8	58.4	59.9
DCCT scale uncertainty (%)	2.7	2.7	2.7
Uncorrelated uncertainty (%)	2.0	2.4	3.7
Cross-section uncertainty (%)	3.4	3.6	4.6
Relative normalization stability (%)	0.5		
Use of average value of $\mu_{\text{vis}}$ (%)	0.5		
Additional uncertainty for other data-sets (%)	0.7		
Total uncertainty for large data sets (%)	3.5		

agreement with the measurement performed with the van der Meer scan method using dedicated fills in April 2010 and October 2010. The VDM method has an overall relative uncertainty of 3.6%. The final VDM result is based on the October data alone which give significantly lower systematic uncertainties. The common DCCT scale error represents a large part of the overall uncertainty for the results of both methods and is equal to 2.7%. To determine the average of the two results the common scale should be removed before calculating the relative weights. Table 10 shows the ingredients and results of the averaging procedure. The combined result has a 3.4% relative error.

Since the data-sets used for physics analysis contain only a subset of all available information (see Sect. 3), a small additional error is introduced *e.g.* by using  $\mu_{\text{vis}}$  information averaged over bunch crossings. Together with the uncertainty introduced by the long term stability of the relative normalization this results in a final uncertainty in the integrated luminosity determination of 3.5%. We have taken the conservative approach to assign a 0.5% uncertainty representing the relative normalization variation to all data-sets and not to single out one specific period as reference. The results of the absolute luminosity measurements are expressed as a calibration of the visible cross-section  $\sigma_{\text{vis}}$ . This calibration has been used to determine the inclusive  $\phi$  cross-section in  $pp$  collisions at  $\sqrt{s} = 7$  TeV [25].<sup>9</sup>

The relative normalization and its stability have been studied for the data taken with LHCb in 2010 (see Sect. 3). Before the normalization can be used for other data-sets an appropriate study of the relative normalization stability needs to be performed.

While the VDM data have been taken during dedicated fills, no dedicated data taking periods have yet been set aside for the BGI method. It is, therefore, remarkable that this method can reach a comparable precision. A significantly improved precision in the DCCT scale can be expected in the near future. In addition, a controlled pressure bump in the LHCb interaction region would allow us to apply the beam-gas imaging method in a shorter period, at the same time decreasing the effects from non-reproducibility of beam conditions and increasing the statistical precision. The main uncertainty in the VDM result, apart from the scale error, is due to the lack of reproducibility found between different scanning strategies. Dedicated tests will have to be designed to understand

<sup>9</sup>In fact, for the early data-taking period on which this measurement is based, the hit count in the SPD is used to define the visible cross-section. This cross-section differs from  $\sigma_{\text{vis}}$  defined in this paper by 0.5%.

these differences better. Finally, it is also very advantageous to perform beam-gas measurements in the same fill as the van der Meer scans. This would allow cross checks to be made with a precision which does not suffer from scale uncertainties in the bunch population measurement. Furthermore, a number of parameters which limit the precision of the BGI method can be constrained independently using the VDM scan data, such as the relative beam positions. To improve the result of the BGI method a relatively large  $\beta^*$  value should be chosen, such as 10 m. The precision of the VDM method does not, in principle, depend on  $\beta^*$ .

## 9. Acknowledgements

We express our gratitude to our colleagues in the CERN accelerator departments for their support and for the excellent performance of the LHC. In particular, we thank S. White and H. Burkhardt for their help on the van der Meer scans. We thank the technical and administrative staff at CERN and at the LHCb institutes, and acknowledge support from the National Agencies: CAPES, CNPq, FAPERJ and FINEP (Brazil); CERN; NSFC (China); CNRS/IN2P3 (France); BMBF, DFG, HGF and MPG (Germany); SFI (Ireland); INFN (Italy); FOM and NWO (Netherlands); SCSR (Poland); ANCS (Romania); MinES of Russia and Rosatom (Russia); MICINN, XuntaGAL and GENCAT (Spain); SNSF and SER (Switzerland); NAS Ukraine (Ukraine); STFC (United Kingdom); NSF (USA). We also acknowledge the support received from the ERC under FP7 and the Région Auvergne.

## References

- [1] M. Mangano, “*Motivations and precision targets for an accurate luminosity determination*”, Proc. “LHC Lumi Days: LHC Workshop on LHC Luminosity Calibration”, CERN-Proceedings-2011-001, CERN (2011).
- [2] J. Anderson, “*Prospects for indirect luminosity measurements at LHCb*”, Proc. “LHC Lumi Days: LHC Workshop on LHC Luminosity Calibration”, CERN-Proceedings-2011-001, CERN (2011).
- [3] R. Thorne, A. Martin, W. Stirling and G. Watt, “*Parton distributions and QCD at LHCb*”, Proc. XVI International Workshop on Deep-Inelastic Scattering and Related Topics, London, England, April 2008, arXiv:0808.1847 [hep-ph].
- [4] F. De Lorenzi, “*PDF sensitivity studies using electroweak processes at LHCb*”, Proc. XVIII International Workshop on Deep-Inelastic Scattering and Related Subjects, Convitto della Calza, Firenze, Italy, arXiv:1011.4260 [hep-ex], 2010.
- [5] C. Møller, “*General properties of the characteristic matrix in the theory of elementary particles*”, K. Danske Vidensk. Selsk. Mat.-Fys. Medd. 23, 1 (1945); for later papers see e.g. O. Napoly, “*The luminosity for beam distributions with error and wake field effects in linear colliders*”, Particle Acc. 40 (1993) 181; W. Herr, B. Murator, “*Concept of luminosity*”, Proceedings of CERN Accelerator School, 361 (2003).
- [6] The TOTEM Collaboration, TOTEM Technical Design Report, CERN-LHCC-2004-002, TOTEM-TDR-001.
- [7] The ATLAS Collaboration, “*ATLAS Forward Detectors for Measurement of Elastic Scattering and Luminosity*”, CERN-LHCC-2008-004, ATLAS TDR 18 (2008).

- [8] S. van der Meer, “*Calibration of the effective beam height in the ISR*”, CERN report, ISR-PO/68-31, 1968 (CERN).
- [9] H. Burkhardt and P. Grafström, “*Absolute luminosity from machine parameters*”, CERN-LHC-PROJECT-Report-1019 (2007).
- [10] M. Ferro-Luzzi, “*Proposal for an absolute luminosity determination in colliding beam experiments using vertex detection of beam-gas interactions*”, Nucl. Instrum. Methods A 553 (2005) 388, CERN-PH-EP-2005-023.
- [11] R. Aaij *et al.*, The LHCb Collaboration, “*Prompt  $K_S^0$  production in pp collisions at  $\sqrt{s} = 0.9$  TeV*”, Phys. Lett. B 693 (2010) 69, CERN-PH-EP-2010-027, arXiv:1008.3105 [hep-ex].
- [12] V. Balagura, “*Luminosity measurements in the first LHCb data*”, V. Balagura, Proc. 2010 Rencontres de Moriond (QCD), La Thuile (2010).
- [13] P. Hopchev, “*The beam-gas method for luminosity measurement at LHCb*”, Proc. 2010 Rencontres de Moriond Electroweak Interactions and Unified Theories, La Thuile (2010), arXiv:1005.4398 [physics.ins-det].
- [14] K. Oyama, “*Analysis of the May 2010 van der Meer scan in ALICE*”, Proc. “LHC Lumi Days: LHC Workshop on LHC Luminosity Calibration”, CERN-Proceedings-2011-001, CERN (2011); ATLAS Collaboration, “*Luminosity Determination in pp Collisions at  $\sqrt{s} = 7$  TeV Using the ATLAS Detector at the LHC*”, Eur. Phys. J. C 71 (2011) 1630, CERN-PH-EP-2010-069, arXiv:1101.2185 [hep-ex]; CMS Collaboration, “*Measurement of CMS Luminosity*”, CMS-PAS-EWK-10-004.
- [15] V. Balagura, “*Notes on van der Meer Scan for Absolute Luminosity Measurement*”, Nucl. Instrum. Methods A 654 (2011) 643, arXiv:1103.1129 [physics.ins-det].
- [16] J. Bossler *et al.*, “*Transverse Emittance Measurement With a Rapid Wire Scanner at the CERN SPS*”, Nucl. Instrum. Methods A 235 (1985) 475.
- [17] The LHCb collaboration, “*The LHCb Detector at the LHC*”, JINST 3 S08005 (2008).
- [18] N.Yu. Zaitsev, “*Study of the LHCb pile-up trigger and the  $B_s \rightarrow J/\psi\phi$  decay*”, CERN-THESIS-2000-043, NIKHEF, Amsterdam (2000).
- [19] J.J. Gras, M. Ludwig and P. Odier, “*The 2010 LHC DC BCT measurement system and its main sources of uncertainties*”, CERN-LHC-Project-Note-432; D. Belohrad, J.J. Gras and M. Ludwig, “*The 2010 LHC ring Fast BCT measurement system and its main sources of uncertainties*”, CERN-LHC-Project-Note-433; D. Belohrad *et al.*, “*Commissioning and first performance of the LHC beam current measurement systems*”, 1st IPAC, Kyoto, Japan, 23–28 May 2010.
- [20] G. Anders *et al.*, “*LHC bunch current normalisation for the April-May 2010 luminosity calibration measurements*”, CERN-ATS-Note-2011-004 (2011).
- [21] C. Ohm and T. Pauly, “*The ATLAS beam pick-up based timing system*”, Nucl. Instrum. Methods A 623 (2010) 558.
- [22] A. Alici *et al.*, “*LHC Bunch Current Normalisation for the October 2010 Luminosity Calibration Measurements*”, CERN-ATS-Note-2011-016 PERF.
- [23] C. Lasseur *et al.*, “*Géométrie du LHC : points caractéristiques, formules de transformation*”, CERN-LHC-Project-Note-95 (1997).
- [24] S. White, “*Determination of the Absolute Luminosity at the LHC*”, CERN-THESIS-2010-139, LAL-10-154, Université Paris-Sud 11 (2010).

- [25] R. Aaij *et al.*, The LHCb Collaboration, *Measurement of the inclusive  $\phi$  cross-section in pp collisions at  $\sqrt{s} = 7$  TeV*, Phys. Lett. B 703 (2011) 267, CERN-PH-EP-2011-106, arXiv:1107.3935 [hep-ex].